



HOST UNIVERSITY: The University of Edinburgh

FACULTY: School of Engineering

DEPARTMENT: Civil and Environmental Engineering

Academic Year 2020-2021

**THIN-FILAMENT PYROMETRY AND ANALYSIS OF EXTINCTION ONSET TEMPERATURES FOR  
ETHYLENE FLAMES ON THE BURNING RATE EMULATOR IN THE INTERNATIONAL SPACE  
STATION**

Ryan M. Venzon

Supervisor(s): Grunde Jomaas

Master thesis submitted in the Erasmus+ Study Programme

**International Master of Science in Fire Safety Engineering**

#### **DISCLAIMER**

This thesis is submitted in partial fulfilment of the requirements for the degree of *The International Master of Science in Fire Safety Engineering (IMFSE)*. This thesis has never been submitted for any degree or examination to any other University/programme. The author(s) declare(s) that this thesis is original work except where stated. This declaration constitutes an assertion that full and accurate references and citations have been included for all material, directly included and indirectly contributing to the thesis. The author(s) gives (give) permission to make this master thesis available for consultation and to copy parts of this master thesis for personal use. In the case of any other use, the limitations of the copyright have to be respected, in particular with regard to the obligation to state expressly the source when quoting results from this master thesis. The thesis supervisor must be informed when data or results are used.

Read and approved,



Ryan M. Venzon

May 11, 2021

## Abstract

The temperature at the extinction onset when flame instability begins was determined through Thin-Filament Pyrometry (TFP) for ethylene flames on the Burning Rate Emulator (BRE), TFP is a technique that converts the intensity of thermal radiation into temperature, and it involves insertion of SiC filaments into a flame. The filaments glow as they emit radiation, and the process is captured by a digital camera that is calibrated to interpret the pixels of the filaments in the image into gas temperature. The four BRE-produced flames analysed with intensity ratio TFP used a 25-mm burner in microgravity environment of the International Space Station. The results of the TFP analysis showed that the extinction onset temperature is 1,168 K, between the 1,100 K and 1,200 K projection and simulation from previous studies. This finding can define more precisely and accurately the flammability range of materials used within spacecrafts. In addition, the TFP-measured temperatures were found to differ by as much as 200-700 K from CEA-calculated temperatures derived from theoretical equilibrium equation and radiometer reading. This discrepancy suggests the necessity of revisiting the assumptions and input parameters used in inferring flame temperature from radiometry. With these findings, a better understanding of the fundamentals of combustion in microgravity is achieved towards the ultimate aim of improving fire safety in spacecrafts.

## Acknowledgements

This master's thesis has been a daunting task from the start because of the specialized and “out of this world” nature of the subject – fire safety in microgravity or outer space. Despite the challenges, I was able to accomplish the tasks at hand and finished writing my thesis, thanks to the valuable help of the Earthlings enumerated below.

Firstly, I like to thank my supervisors, Prof. Grunde Jomaas and Prof. Peter Sunderland, for their guidance. Their expertise and research orientation helped me overcome the obstacles I encountered and provided focus on my analysis and writing.

Also, I extend my gratitude to the other BRE team members: Parham Dehghani for data gathering assistance and tutoring me on CEA program, Anna Wright for orienting me about OMA2 and providing me data for my analysis, Dr. John de Ris for his constructive insights, and Prof. Alexander Snegirev for his inputs from flame simulation.

Additionally, I give thanks to the other researchers, Dennis Stocker for giving me NASA reference documents, Logan Tan for helping me with OMA2 codes, and Kendyl Waddell for assisting me on Matlab program and scripts troubleshooting.

Lastly, I say *merci beaucoup* to Damien, my family and friends for the encouragement and confidence in my capabilities. Your unwavering support keeps the fire burning in me, even during this difficult time of Covid-19 pandemic, so that I can fulfil my goal of becoming a competent fire safety engineer. *Mabuhay* or cheers to life!

# Table of Contents

<i>Abstract</i> .....	<i>ii</i>
<i>Acknowledgements</i> .....	<i>iii</i>
<i>List of Figures</i> .....	<i>v</i>
<i>List of Tables</i> .....	<i>vi</i>
<i>List of Notations</i> .....	<i>vii</i>
<i>Chapter 1 - Introduction</i> .....	<i>1</i>
1.1. Fire Safety in Microgravity .....	1
1.2. Burning Rate Emulator (BRE) .....	3
1.2.1. Flame Characteristics .....	6
1.2.2. Flame Extinction Mechanism .....	7
1.3. Thin Filament Pyrometry (TFP) .....	10
1.3.1. Image Capture .....	12
1.3.2. Image Post-Processing .....	14
1.3.3. Conversion from Intensity to Temperature .....	14
1.4. Aim and Objectives .....	16
<i>Chapter 2 - Methodology</i> .....	<i>18</i>
2.1. BRE Flame Test Set-up and Procedure .....	18
2.2. TFP Gas Temperature Determination .....	21
2.1.1. Flame Selection .....	22
2.1.2. Image Formatting.....	24
2.1.3. Image Subtraction .....	26
2.1.4. Intensity Conversion .....	27
2.1.5. Temperature Correction .....	30
2.3. CEA Gas Temperature Determination .....	32
<i>Chapter 3 – Results</i> .....	<i>34</i>
3.1. TFP Gas Temperature .....	34
3.2. CEA Gas Temperature .....	41
<i>Chapter 4 – Discussion</i> .....	<i>45</i>
<i>Chapter 5 - Conclusions</i> .....	<i>49</i>
<i>References</i> .....	<i>51</i>

## List of Figures

<i>Figure 1: Comparison of actual flame (left) and emulated flame (right) under normal gravity ....</i>	<i>4</i>
<i>Figure 2: BRE-2 flame at different time interval under microgravity .....</i>	<i>5</i>
<i>Figure 3: BRE schematics .....</i>	<i>6</i>
<i>Figure 4: BRE flame test process flow .....</i>	<i>20</i>
<i>Figure 5: TFP process flow.....</i>	<i>21</i>
<i>Figure 6: Comparison of HOBJ (left) and demosaiced, red channel TIFF (right) images .....</i>	<i>25</i>
<i>Figure 7: Comparison of unsubtracted (left) and subtracted (right) TIFF images .....</i>	<i>27</i>
<i>Figure 8: Pixel intensity mapping of a TIFF image .....</i>	<i>29</i>
<i>Figure 9: Peak pixel intensity locations for Flame 1 (left) and Flame 2 (right).....</i>	<i>36</i>
<i>Figure 10: Peak pixel intensity locations for Flame 3 (left) and Flame 4 (right).....</i>	<i>37</i>
<i>Figure 11: TFP gas temperature over time at different filament levels for Flame 1 .....</i>	<i>38</i>
<i>Figure 12: TFP gas temperature over time at different filament levels for Flame 2 .....</i>	<i>38</i>
<i>Figure 13: TFP gas temperature over time for Flame 3 .....</i>	<i>41</i>
<i>Figure 14: TFP gas temperature over time for Flame 4 .....</i>	<i>41</i>
<i>Figure 15: Equilibrium temperature as function of radiative loss fraction for Flame 1 (left) and Flame 2 (right).....</i>	<i>42</i>
<i>Figure 16: Equilibrium. temperature as function of radiative loss fraction for Flame 3 (left) and Flame 4 (right).....</i>	<i>42</i>
<i>Figure 17: CEA gas temperature over time for Flame 1.....</i>	<i>43</i>
<i>Figure 18: CEA gas temperature over time for Flame 2.....</i>	<i>43</i>
<i>Figure 19: CEA gas temperature over time for Flame 3.....</i>	<i>44</i>
<i>Figure 20: CEA gas temperature over time for Flame 4.....</i>	<i>44</i>
<i>Figure 21: TFP gas temperature comparison with CEA gas temperature for Flame 1 .....</i>	<i>46</i>
<i>Figure 22: TFP gas temperature comparison with CEA gas temperature for Flame 2 .....</i>	<i>46</i>
<i>Figure 23: TFP gas temperature comparison with CEA gas temperature for Flame 3 .....</i>	<i>47</i>
<i>Figure 24: TFP gas temperature comparison with CEA gas temperature for Flame 4 .....</i>	<i>47</i>
<i>Figure 25: TFP gas temperature as a function of CEA gas temperature .....</i>	<i>48</i>

## List of Tables

<i>Table 1: Test parameters of BRE design matrix.....</i>	<i>18</i>
<i>Table 2: Characteristics of selected flames.....</i>	<i>24</i>
<i>Table 3: Reaction parameters of self-extinguished (Flame 1 &amp; 2) and fuel-terminated (Flame 3 &amp; 4) flames.....</i>	<i>33</i>
<i>Table 4: Evolution of self-extinguished (Flame 1 &amp; 2) and fuel-terminated (Flame 3 &amp; 4) flames .....</i>	<i>35</i>
<i>Table 5: Projection of extinction temperature for Flame 1 and Flame 2.....</i>	<i>40</i>
<i>Table 6: Sensitivity analysis of extinction onset temperature for Flame 1 and Flame 2 .....</i>	<i>45</i>

## List of Notations

<i>Notations</i>	<i>unit</i>	
A	area	m <sup>2</sup>
C <sub>1</sub>	radiation constant 1	W/m <sup>2</sup>
C <sub>2</sub>	radiation constant 2	m-K
C <sub>3</sub>	camera fitting constant	m <sup>2</sup> -m/W-s
d	diameter	m
E	spectral emissive power	W/m <sup>3</sup>
F	f-number	
FF	Fill Factor	
h	convective heat transfer coefficient	W/m <sup>2</sup> -K
HAB	Height Above Burner	mm
I	pixel intensity	
k	thermal conductivity	W/m-K
$\dot{m}''$	mass flux	g/m <sup>2</sup> -s
n	number of moles	
Nu	Nusselt number	
P	pressure	kPa
$\dot{q}$	theoretical heat release rate	kW
$\dot{q}''$	radiant heat flux	kW/m <sup>2</sup>
t	time of exposure of an image	s
T	Temperature	K
TF	Transmissivity Factor	
u	velocity	m/s
X	molar fraction	
X <sub>r</sub>	radiative loss fraction	

### *Greek notations*

$\alpha$	thermal diffusivity	m <sup>2</sup> /s
$\varepsilon$	emissivity	
$\lambda$	wavelength	m
$\sigma$	Stefan-Boltzmann constant	W/m <sup>2</sup> -K



*Subscripts*

amb ambient

fil filament

fuel fuel mixture

gas gaseous combustion mixture

N<sub>2</sub> Nitrogen

O<sub>2</sub> Oxygen

## Chapter 1 - Introduction

Space exploration and its potential to benefit humanity have been a major interest to many humans and institutions from the time that the first human landed on the moon in 1969, to this year on February 18, when Perseverance rover successfully landed on Mars to help study the planet's habitability in preparation for future manned missions (NASA, 2020). While the benefits can be substantial, the risks involved are also enormous. One of these risks can be a fire incident that can kill astronauts in confined spacecrafts, destroy expensive space equipment, and compromise missions that took years of preparation. As such, fire safety in space exploration must be studied, especially because fire in outer space is starkly different from a fire on Earth.

### 1.1. Fire Safety in Microgravity

Fire properties and characteristics at normal gravity condition on Earth are not similar to what would be observed in microgravity, e.g., inside spacecrafts like the International Space Station (ISS) where gravitational forces are weak at  $<1 \mu\text{g}$ . On earth, gravity affects flames strongly because the hot combustion gases are much less dense than the cooler atmospheric gases. Gravity causes the hot gases to move upward as it pulls more strongly on the denser atmosphere, in a phenomenon called buoyancy. This buoyancy causes upward air entrainment towards a flame, making the flame elongated and flickering, and removes the combustion products away. On the other hand, lack of buoyancy in space makes the flame look dome-like and non-flickering or quasi-steady (Chao *et al.*, 2015).

In addition to the flame appearance, there are other differences in microgravity flame compared to normal-gravity flame. Microgravity flames are more sensitive to its environment and has broader characteristics because of the absence of buoyancy-induced entrainment. It also has longer length scales and residence times that can easily facilitate the study of flame structures, soot formation, stability mechanism and reaction kinetics (Chao, 2015). Such research findings in microgravity flames can also be applied in understanding normal-gravity flame properties which cannot be observed or quantified under normal Earth conditions.

Fire research under the Aeronautics and Space Administration (NASA) of the United States of America (USA) has been ongoing since 1980s. Earlier studies have largely focused on applied research to solve practical problems in spacecrafts. However, more recent studies have focused on fundamental research to understand better the combustion science in space (NASA, 2013).

An example of this research is the Advanced Combustion via Microgravity Experiments (ACME), formalized in 2013. ACME consists of five independent experiments on laminar, gaseous diffusion flames in ISS. Four of the experiments are aimed at addressing environmental concerns like pollution control and energy problems such as improving the efficiency of combustion systems, through the development or improvement of computational models. The fifth experiment, called the Burning Rate Emulator (BRE), is concerned about fire safety, principally for space vehicles. The focus of BRE study is fire prevention in spacecrafts. Particularly, its objectives are to understand the fundamental flammability properties of materials, such as ignition and extinction,

and to verify the applicability of existing flammability test methods in microgravity settings (NASA, 2013).

## **1.2. Burning Rate Emulator (BRE)**

Studying the flaming behavior of various solid and liquid materials, hereafter referred to as 'condensed fuels', gives valuable data in qualifying if such materials are safe to use inside spacecrafts like the ISS. However due to the vast number of condensed fuels available, it is very time-consuming and costly to study each and every one of them. Therefore, a system has to be developed to approximate the flame properties of condensed fuels without actually doing experiments on them. While the system is simpler, the data has to be reliable and realistic as well.

Such experimental system has already been developed through the years under the stewardship of NASA. The system is called the Burning Rate Emulator (BRE). As its name implies, the BRE is a type of burner that emulates or approximates the flame appearance of various condensed fuels by burning only a limited number of gaseous fuels with controlled properties and under defined conditions. BRE has been used initially for experiments under normal gravity but later, the experiments were performed under microgravity conditions.

For a certain condensed fuel, a range of values for four properties are established through experiments. These properties are heat of gasification, heat of combustion, surface temperature

and smoke point. Burning this condensed fuel at these conditions produces a flame with specific appearance and height. By setting the mentioned properties in a gaseous fuel to the same range of values, a similar looking flame is produced. This is when the flame of the condensed fuel is said to be 'emulated'.

The emulation experiments using BRE started in 2015 (Zhang *et al.*, 2015) when flames of four condensed fuels were effectively emulated under normal gravity. The experiments used BRE-1, the prototype of the burner that is made of perforated brass surface and equipped only with heat flux sensors. Figure 1 shows the actual flames from condensed fuels in comparison with the emulated flames using gaseous fuels.

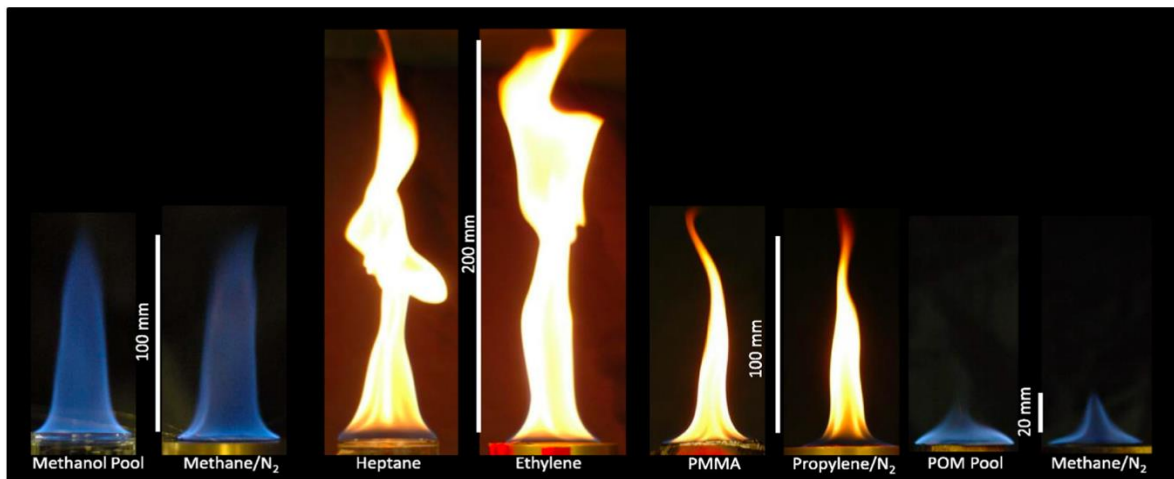
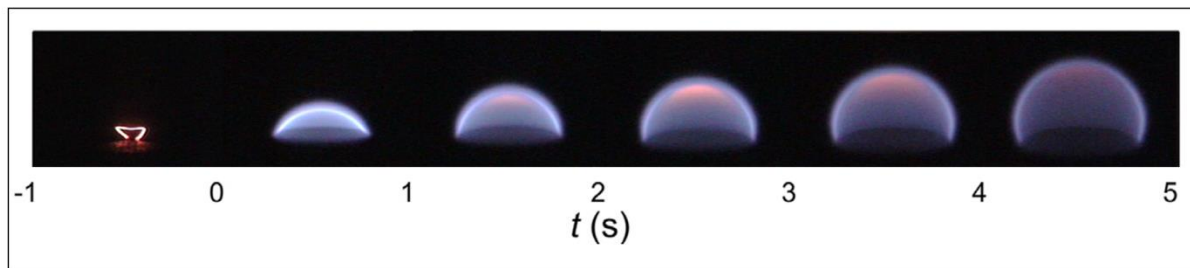


Figure 1: Comparison of actual flame (left) and emulated flame (right) for a number of fuels in normal gravity using BRE-1 (Zhang, 2015)

Further development led to BRE-2 that is made of perforated copper surface embedded with thermocouples. This improvement allowed calorimetry to measure the heat flux more accurately as demonstrated in succeeding experiment (Markan *et al.*, 2018). Unlike BRE-1, the BRE-2

experiments were performed under microgravity conditions using the drop tower at NASA Glenn's Zero Gravity Research Facility. Typically, the duration of the experiments were about five seconds only because of the inherent complexity of generating microgravity in the drop tower. Figure 2 shows photographs from one of these experiments.

Nonetheless, even if longer microgravity experiment is possible using a research aircraft flying parabolically, the quality of microgravity generated is not conducive for low-momentum flames like BRE flames: the disturbance in gravity or "g-jitter" in the aircraft can disturb the flame considerably, and avoiding this by floating the experiment reduces the test duration to mere seconds (Stocker *et al.*, 2014) .



*Figure 2: BRE-2 flame at different time intervals in microgravity generated from drop tower experiment (Markan, 2018)*

BRE-3 is the latest version of the emulator, and schematics of it is shown in Figure 3 . It has similar design as BRE-2, and the experiments were not Earth-based but performed on board the ISS since 2019. Without the limitation in generating longer and good quality microgravity, longer and more comprehensive experiments were able to be done. The first round of BRE-3 experiments was done in February to April of 2019. Afterwards, the second and latest round of BRE-3 experiments

was performed from September 2020 to January 2021. This round, consisting of 139 tests, will be the focus of this thesis.

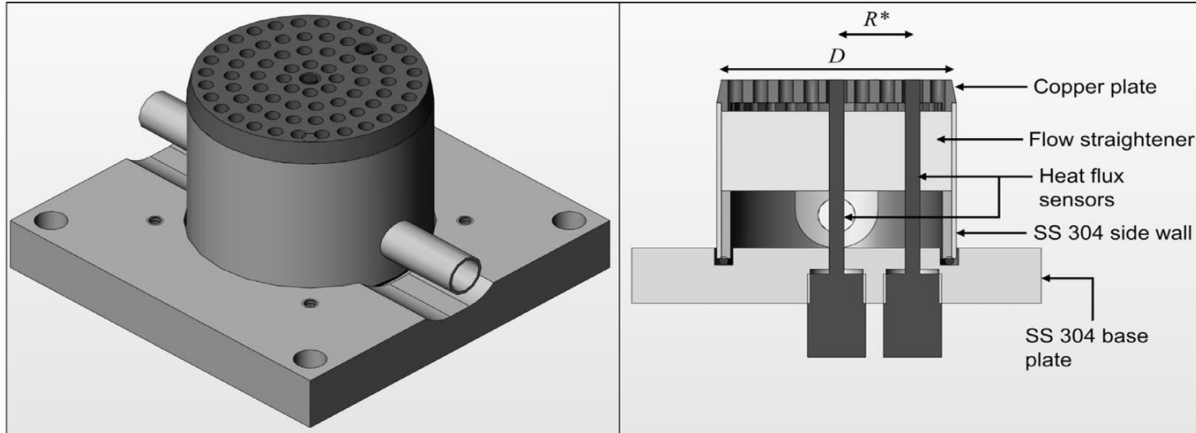


Figure 3: BRE-3 schematics, showing top surface perforations (left) and side-view cut-out of the internals (right) (Markan, 2018)

### 1.2.1. Flame Characteristics

The flame produced from BRE in microgravity is a low momentum or laminar diffusion flame that is axis-symmetrical and can be described as “dome-shaped or more accurately, ellipsoidal. An analytical solution that predicts the transient flame shape and heat flux of the BRE-2 flames had been developed with good agreement (Markan *et al.*, 2020). The same solution had been the basis of characterizing the “steadiness” of BRE-3 flames, to differentiate if they are non-steady that tend to self-extinguish or not. The non-steady, self-extinguishing flames were observed to be periodically grow after ignition, then eventually decay up to the point of extinction. For the “steady” flames (in quotation to mean near-steady at the endpoint of the flame test), sustained burning of bluish flame is observed for more than three minutes (Dehghani *et al.*, 2021).

### 1.2.2. Flame Extinction Mechanism

There are many types of flame extinction mechanism for a diffusion flame. Aerodynamic quenching happens when the flame residence time is reduced by flow-induced disruption. Another is thermal quenching which weakens a flame by convective or radiative loss. On the other hand, dilution quenching happens when the fuel and oxygen mixture is changed (Lecoustre *et al.*, 2011). For the BRE flames in microgravity, the extinction mechanism observed is thermal quenching by radiative loss (radiative extinction) primarily because of the low strain rates with longer residence times (Santa *et al.*, 2007).

The BRE-3 round one flames had been subjected to three-dimensional simulation to study the transient mechanisms of their radiative extinction in microgravity (Snegirev *et al.*, 2020). The simulation confirmed the experimental observation of flame growth after ignition, then reaching a point of instability which eventually leads to extinction. Figure 4 below illustrates this transient mechanism.

Initially, the flame grows in volume, accompanied by a progressive drop in temperature. This temperature reduction is primarily because of the increased volumetric radiative losses over time as opposed to the generation of heat of combustion which is limited on the flame's outer surface.

When the temperature drops low enough, the flame's upper part experiences a localized extinction which is seen as a large hole. At the same time, the other parts of the flames



oscillate or begin to move up and down periodically. This point is referred to as the “extinction onset.”

After some time, the flame recovers when a stratified combustion mixture builds up at the top which then reignites and propagates upward to retain the starting flame shape. However, the flame is not a unified, homogeneous volume but rather characterized as several “triple flame” consisting of three arms: one fuel-rich premixed flame, one fuel-lean premixed flame, and a trailing diffusion flame all emanating from one point or head (Juanós and Sirignano, 2014).

The heads eventually collide, causing a sudden increase in heat release rate and decrease in flame strength. This phenomenon is repeated until the flame becomes too weak and quenches totally.

Given what we know so far about the BRE-3 flames characteristic and extinction mechanism as observed from a reduction in temperature over time, it is worth investigating if the temperature measurement is accurately done. The BRE team has inferred flame temperature through radiometer reading hitherto, and while the simulation result can provide approximate value, this largely depends on the combustion model used. A more direct measurement of flame temperature is thus needed, to help firm up the extinction phenomenon observations and the safety guidelines that can be produced from these observations.

The flame temperature can be directly determined through pyrometry, a method of measuring temperature by relating it to the thermal radiation emitted from a hot object. The temperature

is captured by a device called pyrometer or “radiation thermometer” in simplified term (Glückert, 1994). Specifically, Thin-Filament Pyrometry or TFP will be employed for this thesis. As its name implies, filaments or thin, thread-like materials will be used as pyrometer: they will be positioned within the flame and the intensity of their radiant glow can be interpreted as temperature.

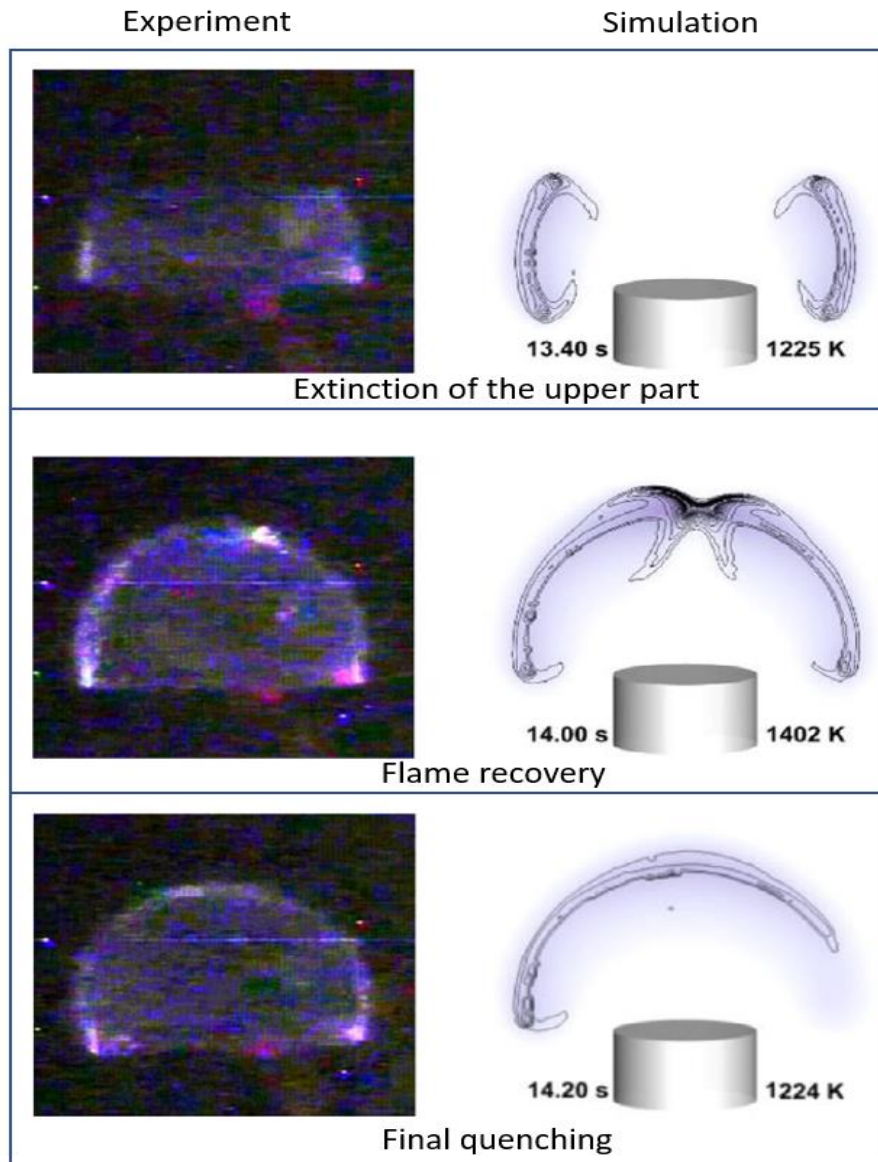


Figure 4: Transient disintegration and quenching of BRE-3 flame (Snegirev, 2020)

### 1.3. Thin Filament Pyrometry (TFP)

Radiation is the energy emitted by a body in the form of electromagnetic wave, characterized by its wavelength or frequency, and a longer wavelength (lower frequency) means a lower radiative energy. Particularly for thermal radiation, or the energy emitted because of a body's temperature, the wavelength falls within 0.1 to 100  $\mu\text{m}$  encompassing the infrared, visible light and ultraviolet regions (Çengel, 2007).

At room temperature, the molecules, atoms and electrons of a body move slowly, and the thermal radiation falls within the infrared region. When additional heat is applied to a body, its atoms and electrons move faster, and the thermal radiation enters the visible light region with wavelength of 0.40-0.76  $\mu\text{m}$ . Further below this wavelength range, the thermal radiation falls within the ultraviolet region. However, only the visible light region can be seen by the naked eye, allowing visual interpretation of the temperature of a hot body such as a flame. Therefore, for TFP application to flame, only the visible light region of thermal radiation is considered.

The TFP for temperature analysis of a flame has been ongoing since 1980s, when Silicon Carbide (SiC) filaments were proposed for TFP. SiC was deemed more suitable for flame application because of its inertness in oxidizing condition, relatively high emissivity and lower conductivity compared to metal alloys used in thermocouple (Vilimpoc and Goss, 1988). The principal idea is that the SiC filament must be positioned crossflow, within the flame's burning gas region and assumed to reach a steady-state heat transfer, chiefly by radiation, between the filament and the gas. Then, heat balance to account for losses is performed to correct the measured filament temperature to the required gas temperature.

At flame temperature greater than 1,000 K, temperatures that can be expected from BRE flames, the heated SiC filament (fil) glows or emits thermal radiation in the visible light region. The higher the temperature, the brighter the glow becomes. This brightness of glow is what is known as the spectral emissive power  $E_\lambda$ , defined as the radiation emission rate of a specific wavelength ( $\lambda$ ) per surface area, per unit wavelength in all directions. For a radiating body of  $\lambda$  and temperature (T), the  $E_\lambda$  is computed from the Planck's equation as shown in Eq. 1:

$$E_\lambda = \varepsilon C_1 / \left[ \lambda^5 \left( \exp \left( \frac{C_2}{\lambda T} \right) - 1 \right) \right] \quad (1)$$

The  $E_\lambda$  is in  $W/m^3$ ,  $\lambda$  in meter, T in K, and the radiation constants are  $C_1=3.742 \times 10^{-16} W/m^2$  and  $C_2=1.439 \times 10^{-2} m \cdot K$  (Chhabra and Shankar, 2018). The emissivity ( $\varepsilon$ ) can either be 1 for an idealized black body, or less than unity as in the case of a SiC filament which is typically considered as a grey body with surface properties that are independent of its wavelength.

Since the objective of TFP is finding the temperature, the Planck's equation above can be transposed with the temperature as the unknown and then determined experimentally. The determination is done with a digital camera, especially calibrated to enable the translation of the pixel intensity of the filament's digital image into  $E_\lambda$ . Furthermore, the camera settings must be controlled to enable precise quantification of pixel intensities.

### **1.3.1. Image Capture**

A digital camera forms an image by capturing the radiation from an object into a surface that is sensitive to radiation. Typically, the surface is a photosensor that convert the radiation into electrical signals which are then assigned with numbers. Next, these numbers are inputted to an image processor that converts them into pixels, the smallest image element that contains information about brightness (luminance) and color (chrominance). Particularly, the color is normally filtered into the basic color channels of red, green and blue.

The photosensor is one of the most important components of a digital camera and is generally of two types: Charge-Coupled Device (CCD) or Complementary Metal-Oxide Semiconductor (CMOS). The CCD signal conversion happens at each photosensor while the CMOS converts in groups through a common output amplifier. Thus, the CCD has higher dynamic range and very low noise level but more costly (Franceschetti, 2012). Such CCD camera is used for TFP, hereafter referred to as ACME Data Camera, because of the high quality required for quantitative analysis of the flame's images.

In particular, the ACME Data Camera has a brand name of Navitar KOWA LMZ45T3 Zoom Lens. It is a 1.4-megapixel CCD, digital color camera. Its lens is motorized and allows control over zoom, focus and iris (NASA, 2016). Its exposure and photosensor's gain can also be specified. The precise control of these camera settings – zoom, focus, iris, exposure and gain – is crucial to produce images having representative pixel values with minimal distortions.

Aside from the precise camera control, equally important is the disabling of automatic image enhancement features of the ACME Data Camera. These features may be important for an ordinary snapshot camera to enable quick and easy viewing of the image after it was taken. However, they will invalidate the assumption that the electrical signal has linear relation with the radiation intensity (Kuhn *et al.*, 2011), or more specifically,  $E_\lambda$ . As such, the output from the ACME Data Camera is in raw format, specifically in a lossless binary file format called Halcon Iconic Object (HOBJ) without any enhancement in sharpness, contrast, color and other features. Nevertheless, these HOBJ files will still need post-processing, as will be discussed in the next section, but it will be outside the camera's functionality.

After specifying the camera settings, disabling the enhancements and post-processing the image, it can be assumed that the electrical signal, or pixel intensity ( $I$ ) after going through the camera's processor, is linearly related to  $E_\lambda$  using the following Eq. 2:

$$E_\lambda = \frac{If^2}{tC_3} \quad (2)$$

The  $f$  is the camera's f-number which is a function of the camera's zoom and iris. The  $t$  in  $s$  is the exposure time for the image. On the other hand,  $C_3$  is set at  $2.38 \times 10^{-5} \text{ m}^2\text{-m/W-s}$ , a fitting constant that represents the camera's sensitivity and lens specification. Essentially,  $E_\lambda$  is a normalized  $I$  with respect to the camera parameters mentioned. After linking Eq. 1 and Eq. 2, the  $I$  of the filament's image can now be used to determine the filament temperature ( $T_{\text{fil}}$ ) at its surface, as illustrated in this Eq. 3.

$$T_{\text{fil}} = C_2 / \left[ \lambda \ln \left( \left( \frac{\epsilon_{\text{fil}} C_1}{\lambda^5} \right) \left( \frac{t C_3}{I f^2} \right) + 1 \right) \right] \quad (3)$$

### **1.3.2. Image Post-Processing**

Colored images in their HOBJ raw format are typically not useful for research purposes. For instance, an image of an object of interest may be taken with a background noise that distorts the visual quality. Furthermore, oversaturation of colors in the image can give pixel numbers that are out of bounds, leading to false image analysis. Distortions because of inappropriate camera settings will also produce the same effect.

As such, raw digital images have to be post-processed to enable accurate quantitative analysis. This is done using tools like the Optical Multi-channel Analyzer 2 (OMA2), a program created for the analysis of images for scientific applications like laser-based imaging and spectrophotometry (Kalt P.A.M., 2019). Among various functionalities, OMA2 can display images in different formats and doing simple or complex transformations. These OMA2 capabilities are utilized in this thesis to format and clean the images taken by the ACME Data Camera so that further analysis using TFP can be done.

### **1.3.3. Conversion from Intensity to Temperature**

The pixel intensity's conversion to filament temperature is the heart of the TFP process. This can be done in different ways, the most common of which are the color ratio TFP and intensity ratio TFP. The color ratio TFP, a more recent and simpler technique, relies directly on the ratios of the different color channels to convert into temperature, without the need for calibration. On the other hand, the intensity ratio TFP is the classic technique that requires

calibration and hence, the accuracy of its results can be validated. This Intensity Ratio TFP will be utilized for this thesis.

In intensity ratio TFP, the ratio of the signal at measuring temperature over the signal at a reference temperature is determined. The ratio can be numerically solved by integrating Planck's equation over the spectral response of the photosensor. Typically, the reference temperature is defined through a calibration step that relates known filament temperatures to measured signals to quantify the optical throughput of the camera (Ma *et al.*, 2014). For the ACME Data Camera, a blackbody furnace was used as calibration source. Blackbody images were captured at 1,073-1,473 K in increments of 50 K. At each temperature, the camera settings are adjusted so that the resulting images are just below saturation or maximum pixel intensity.

The computed filament temperature is expectedly lower than the actual gas temperature because of losses to surroundings, so correction has to be made for this. This temperature correction, together with intensity conversion to filament temperature, is executed using Matlab (Matrix Laboratory), a program for iterative assessment and design processes using a language that directly expresses matrix and array mathematics (MathWorks, 2021). Since TFP involves the examination of an array of pixels in different channels, Matlab is highly suitable tool for TFP analysis.



#### **1.4. Aim and Objectives**

The overall, broader goal of this thesis is to contribute to the fundamental understanding of fire safety in microgravity. Previously, the understanding of flames in reduced gravity conditions depends on Earth-based experiments with limited duration and application, primarily because reduced-gravity conditions with enough duration and good quality are difficult to achieve on Earth. Currently, with experiments already made possible in the ISS, the experiments are longer and techniques like TFP can already be performed.

In particular, the TFP has the aim of measuring the temperature of the flames from the BRE-3 (from now on will be referred to only as “BRE” for brevity) round two experiment. The measurement can validate data from previous experiment, enable better understanding of the link between temperature and radiative extinction, and ensure the reliability of safety guidelines that rely on temperature inputs such as flammability limits. The actual experiments were already performed by the astronauts inside the ISS, so sadly no actual experimentation is done in the outer space by the author. Consequently, only data processing and interpretation is done, primarily through intensity ratio TFP.

The temperature determined using intensity ratio TFP can be considered as “true temperature”, because the other methods indirectly determine temperature through secondary measurements like radiometry or flame simulation. The other methods have considerable uncertainty, introduced from the measuring instrument, correlations used in computing the temperature from the measured parameter, or from the simulation model parameters. If the “true temperature” is determined, the uncertainties can thus be corrected or minimized.

Considering the above concerns on temperature uncertainty and its impact on safety guidelines based on temperature inputs, the objective of this thesis is to answer the following fundamental questions about flames in microgravity:

1. What is the temperature that indicates flame extinction?
2. Is the true temperature indicated by radiative loss fraction?

During the flame evolution, the extinction is of special interest because it provides a definite reference point on which to analyse other flame properties and characteristics. Particularly, the start of extinction (Ext) is important to analyse because it indicates when the flame stability ends, and extinction begins. On the other hand, the true temperature as measured from TFP can validate the temperature inferred from radiative loss fraction, and thus provide insight on how to accurately utilize radiometry in temperature measurements.

## Chapter 2 - Methodology

### 2.1. BRE Flame Test Set-up and Procedure

The round two BRE flame tests were performed inside a combustion chamber with a quiescent environment and maintained level of oxygen ( $O_2$ ). The level is expressed as  $X_{O_2}$  or mole of oxygen ( $O_2$ ) over the total moles of  $O_2$  and its Nitrogen ( $N_2$ ) diluent. Additionally, the pressure (P) in the chamber is kept constant throughout each flame test. Likewise, the flow rates of the fuel and its  $N_2$  diluent are controlled to maintain fuel mass flux ( $\dot{m}''$ ) and fuel molar fraction,  $X_{fuel}$ , or moles of fuel over the total moles of fuel and  $N_2$ ; the fuel can either be Methane ( $CH_4$ ) or Ethylene ( $C_2H_4$ ). Lastly, the burner can either be a 25-mm or 50-mm type, based on the burner's nominal diameter. Out of the different combinations of the above test parameters, a design test matrix consisting of 139 tests had been proposed, 130 of which had been successfully ignited. The ranges of the test parameters are summarized in Table 1 below:

*Table 1: Test parameters for the BRE design matrix*

Test Parameter	Minimum	Maximum
$X_{O_2}$	0.21	0.40
P, kPa	57	101
$\dot{m}''$ , g/m <sup>2</sup> -s	1	12
$X_{fuel}$	0.1	1.0

The BRE flame test experiments were performed following the steps summarized in Figure 5, adapted from the operating sequence taken from ACME requirement document (NASA, 2013).

Firstly, the fuel piping to the burner was flushed by setting a small flow of fuel at the  $X_{\text{fuel}}$  concentration to remove residual fuel from previous test.

Next, the combustion chamber P and  $X_{\text{O}_2}$  were established, either by maintaining conditions from previous test if similar, scrubbing and replenishing, or complete evacuation and recharging.

Afterwards, the chamber contents were allowed to reach equilibrium. Typically, a holding time of five minutes is recommended for a quiescent system.

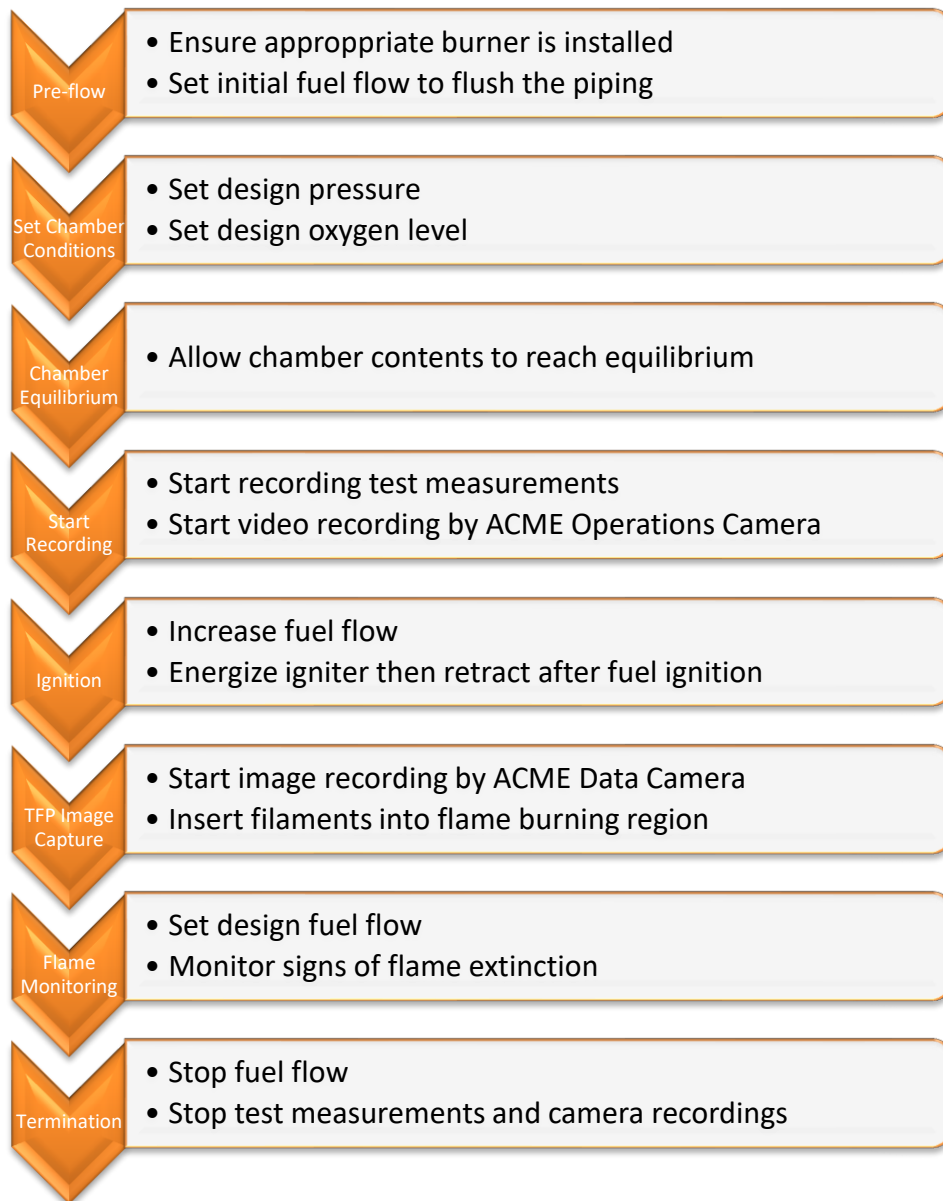
Then, the recording of test parameters and video were started. Note that videos were taken through a separate camera called ACME Operations Camera that captures video of the entire test set set-up, unlike the ACME Data Camera that is focused only on images of the flame and filaments.

The fifth step was the flame ignition, when fuel flow was increased and then ignited with a retractable ignitor, which had to be removed to avoid interference with camera recordings. However, an indication of non-ignition would bypass the sixth step towards the last step; the earlier steps would be repeated for a re-ignition attempt at different fuel flow setting.

When continuous burning was confirmed after ignition, the sixth step involved initiation of ACME Data Camera recording of flame images, raw inputs for TFP analysis. After a few seconds, the TFP filaments were inserted into the flame's burning region and allowed to settle in place.

The seventh step involved continuous flame monitoring, while maintaining the design conditions and flow rates, to enable real-time detection of flame extinction when the burner surface temperature goes below a critical temperature of 573 K.

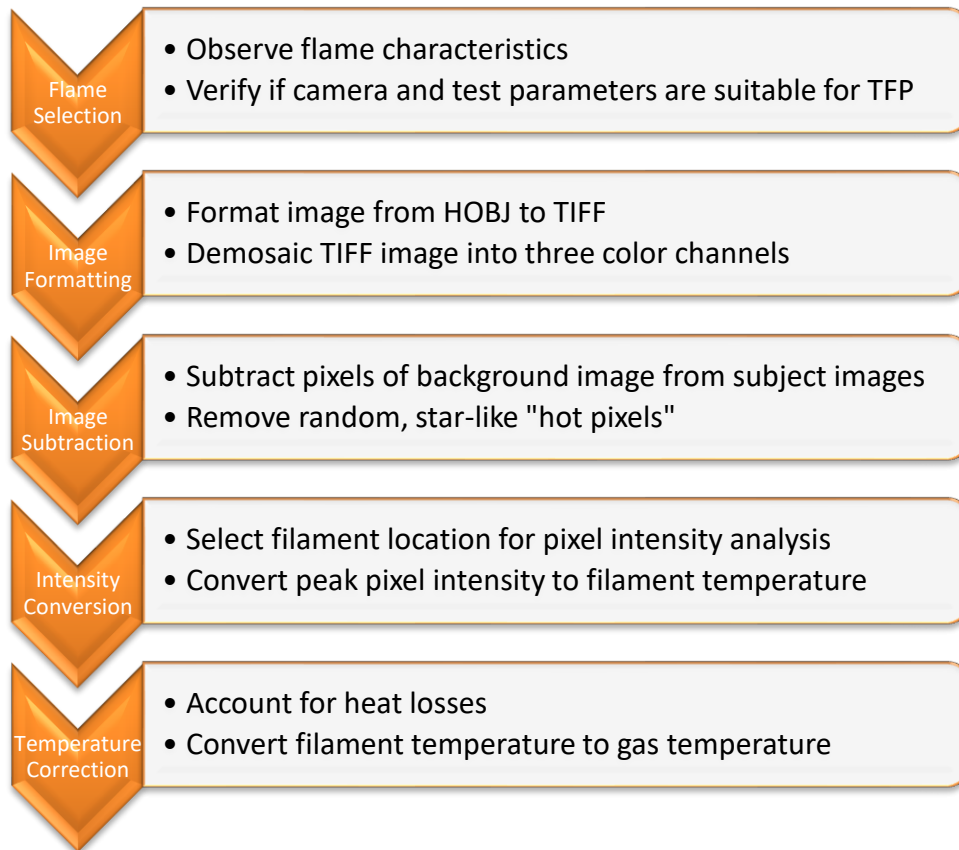
Finally, the flow rates and camera recordings were terminated after extinction had been detected or enough data had been generated for “steady”, non-extinguishing flames.



*Figure 5: BRE flame test process flow*

## 2.2. TFP Gas Temperature Determination

The TFP process consists of five steps outlined in Figure 6. These tasks were performed sequentially, starting with selecting the flames suitable for TFP. Next, the flame's images must be readied for quantitative pixel analysis by formatting and subtracting or removing background distortions. After which, the pixel intensities could already be converted to filament temperatures and finally corrected to gas temperatures (also called "TFP gas temperatures" to differentiate from temperatures calculated using other methods).



*Figure 6: TFP process flow*

### **2.1.1. Flame Selection**

Out of the 130 successfully ignited flame tests, four were chosen for TFP analysis. These flame tests were selected because their camera settings are reliable. For instance, flames are excluded when their images are overexposed or have exposures that do not comply with the specified setting. Furthermore, the flames should have radiometer readings that are not maximized or saturated so that proper correlation with TFP results can be done. Lastly, the flames should have durations that are long enough to allow the different flame stages to occur non-simultaneously with sufficient time gaps. For example, after ignition, the filaments are inserted into the flame and allowed to settle in their locations. The flame extinction onset or beginning of instability should come later, then followed by the flame extinction. If these stages occur without time gaps, the images will have pixels that have overlapping variability in space, time and intensity that will be difficult to quantify.

These initial steps of flame selection involve looking into the raw HOBj files. For one flame, there are around one thousand to four thousand images, depending on the duration of burning. A cursory look on some of the images is confirmed by a more detailed inspection of the ACME Data Camera “mdipsug” file, a recording of the actual camera parameters for each image. Particularly, the actual exposures should follow the specified bracketed exposure settings of 0.005, 0.010, 0.020 and 0.040 s. Bracketed exposure means that for a series of four images, the first image will start with an exposure of 0.05 s, and the next images will have an exposure that is twice longer than the previous image and so on. The succeeding group or “bracket” of four images will follow the same pattern. This bracketing gives

flexibility in TFP so that if the pixel values of images are found to be saturated at 0.040 s, the lower exposure values can still be used.

For the radiometry or measurement of radiant heat flux from the flames, a separate “data” file must be inspected. This file is a recording of the actual, non-imaging, test parameters such as flowrate, temperature, pressure and heat flux. Specifically, the radiant heat flux detected by a radiometer should be within the range of the device, to allow accurate computation of the radiative loss from the flame. Eventually, the equilibrium temperature can be computed and compared against the TFP temperature results.

In addition, the flame characteristics should be verified thru the video recording from the ACME Operations Camera. Through the video, the flame evolution can be observed and used to validate the camera and test parameters. Lastly, the flame tests must be selected if their fuel type is  $C_2H_4$  and burner diameter is 25 mm only, because these are the most used types in the experiments. The other fuel type of  $CH_4$  and burner diameter of 50 mm are not considered, and no attempt is made to compare results against these variables.

In summary, the selected four flame tests are identified in Table 2. Flame 1 and Flame 2 are “self-extinguished”, with inherent flame instability that leads to extinction by itself. With respect to the ignition time, the time when the flame starts to show disturbance from the sustained dome shape is recorded as the extinction onset time, while the moment the flame completely disappears is recorded as the extinction time. The extinction onset and extinction times are determined through video observation and validated from radiometry readings which start to fluctuate at extinction onset and stagnates at extinction.



On the other hand, Flame 3 and Flame 4 are “fuel-terminated”, meaning that for the entire duration of the test, the flame is “steady”, oscillation is not detected, and extinction is initiated only by terminating the fuel source. Thus, no defined extinction onset time and extinction time are recorded for these flames.

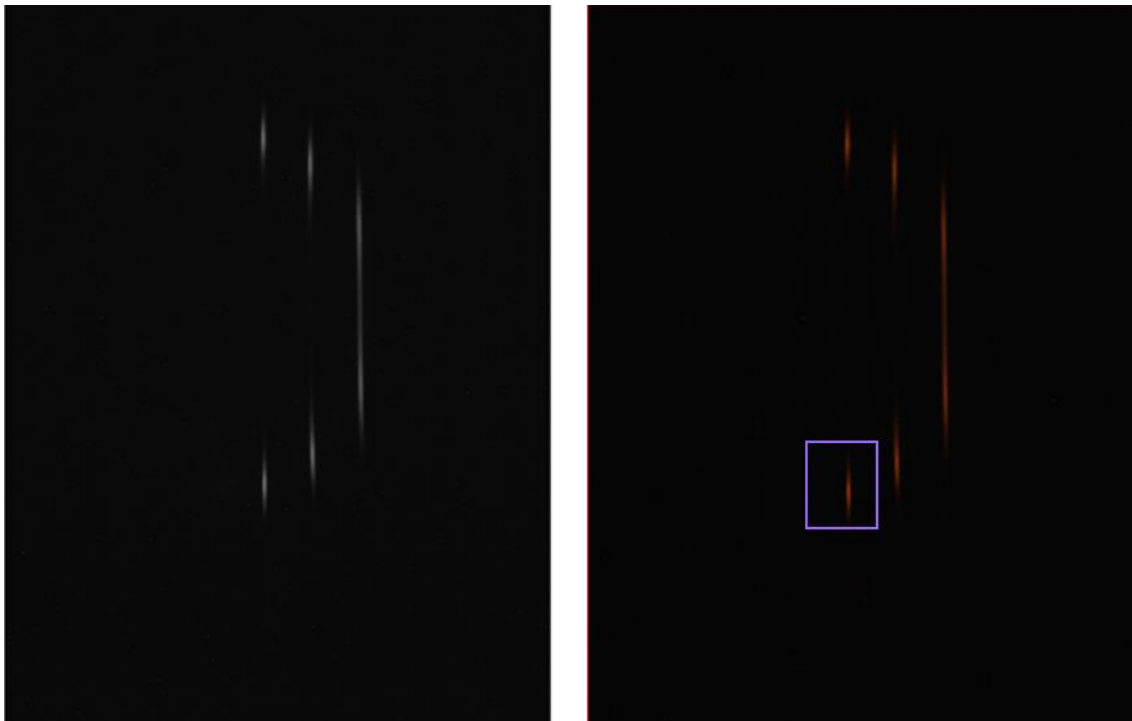
*Table 2: Characteristics of selected flames*

Flame Identification	Test Identification	Extinction onset Time, s	Extinction Time, s	Mode of Extinction
Flame 1	21020D1	63.26	74.34	self-extinguished
Flame 2	20358G2	25.01	32.67	self-extinguished
Flame 3	21020A1	-	-	fuel-terminated
Flame 4	20346A5	-	-	fuel-terminated

### 2.1.2. Image Formatting

The images taken from the ACME Data Camera are in raw HOBJ format that is not readily readable and if viewed using special software is generally in grayscale pixels that do not provide useful quantifiable information. As such, the HOBJ images must be demosaiced into different color channels and formatted into bitmapped image format called Tagged Image File Format (TIFF) using the OMA2 program. The TIFF Format is easily readable and contains only pixel intensity values (or bits) whose locations are identified (or mapped) in a rectangular grid or array, and therefore suitable for TFP application.

As an example, images of Flame 1 at HOBJ format and converted TIFF Format are shown in Figure 7. The left HOBJ image is in grayscale only in an array of 1024 and 1360 horizontal and vertical pixels, respectively. The right image is a demosaiced TIFF image, also at 1024x1360 pixels, but only showing the true color channel of red. The other color channels of green and blue also have 1024x1360 pixels each but they are not shown because they are not used in the calculations. Only the red color channel is used because it has the highest signal-to-noise ratio: it gives the highest pixel values of the filaments and the influence of background pixel values or “noise” is negligible to affect the computations. The detail of the TIFF image, as highlight in the purple box, will be discussed in the next paragraph.



*Figure 7: Comparison of HOBJ (left) and demosaiced, red channel TIFF (right) images*

### 2.1.3. Image Subtraction

Figure 8 shows a TIFF image, a grabbed area from the previous figure, before and after the subtraction process. At the left is the unsubtracted image that still contains background distortions. The filament's background, although it appears black (pixel value = 0), still has some minimal pixel values that need to be subtracted from the subject images so that a base pixel values is established. The last image after flame extinguishment, at the same exposure as the subject images, is taken as the background image and its pixel values are subtracted from the pixel values of each of the subject images.

In addition, the star-like dots that randomly appear in the image must be subtracted as well. These dots are called "hot pixels" that are caused by the radiation damage on the photosensors of the ACME Data Camera; the damage is gradual so that these "hot pixels" increase over time while the camera stays in space orbit. After removing these "hot pixels", the final subtracted image comes out with highly visible filament and deep black background.

The OMA2 program was used as well to perform subtraction operation. It has built-in function to subtract a background image from the subject images. Furthermore, any "hot pixel" can be traced so that if its pixel value differs from the average values of its neighboring pixels by a specified limit, it will automatically be assigned a pixel value of zero. These OMA2 functionalities, among others, are highly valuable for TFP since they automate the time-consuming task of looking at every pixel of each image for analysis.

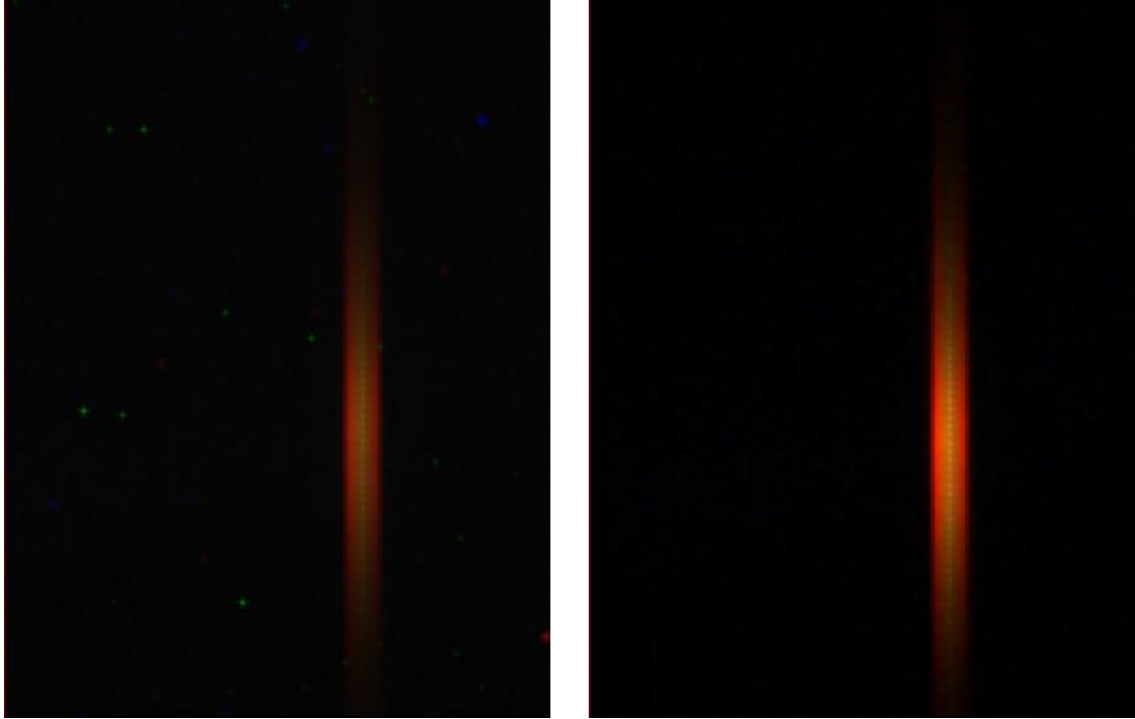


Figure 8: Comparison of unsubtracted (left) and subtracted (right) TIFF images

#### 2.1.4. Intensity Conversion

To recall, the pixel intensity's conversion to fiber temperature is done using Eq. 3 below:

$$T_{\text{fil}} = C_2 / \left[ \lambda \ln \left( \left( \frac{\epsilon_{\text{fil}} C_1}{\lambda^5} \right) \left( \frac{t C_3}{I f^2} \right) + 1 \right) \right] \quad (3)$$

The  $T_{\text{fil}}$  is in K while  $I$  is unitless and expressed as a ratio of the actual pixel value and the maximum, saturated value of 65,536 ( $2^{16}$  for a 16-bit TIFF image). The radiation constants are  $C_1 = 3.742 \times 10^{-16}$  W/m<sup>2</sup> and  $C_2 = 1.439 \times 10^{-2}$  m-K.  $C_3$ , the camera's fitting constant for sensitivity and lens specification, is set at  $2.38 \times 10^{-5}$  m<sup>2</sup>-m/W-s. The emissivity ( $\epsilon_{\text{fil}}$ ) is 0.88 for SiC filament. The  $\lambda$  is  $6.3 \times 10^{-7}$  m for the camera's red response. The  $t$  is chosen to be 0.04 s, the highest of the bracketed exposure settings when the pixel intensities are highest but not

saturated. Meanwhile, the  $f$  is computed from the camera's iris setting, with iris value of 0 for all the four test flames giving an  $f=2.5$  based on the camera's calibration.

With the values of the parameters already given or computed, only the  $I$  value is theoretically needed to compute for  $T_{fil}$ . However, two additional factors are considered in the computation: the filament's Fill Factor (FF) and the camera's Transmissivity Factor (TF). The FF is defined as the unheated filament's size in the image in pixels. The FF is computed from the camera's zoom setting, with zoom value of 30,000 for the four test flames giving an  $FF=0.26$  based on the actual filament's diameter of  $1.4 \times 10^{-5}$  m and camera's calibration. On the other hand, the TF of 0.36 accounts for the reduction over time in the camera's sensitivity and transmittance of optical path with reference to the time of the camera's calibration. Consequently, these factors are inputted as additional parameters to correct the  $I$  value as will be demonstrated below.

Figure 9 is an illustration of one image of a BRE flame. It is assumed that the burner is positioned at the left of the image at  $X$  (horizontal pixel location) of zero. The actual filament locations are shown as Height Above Burner (HAB). Notice that there are three levels of filaments but only the  $HAB=7.8$  mm and  $HAB=12.5$  mm levels are appropriate for TFP analysis. These levels closest to the burner each have two separate areas with red pixels, which means that the filaments crossed the flame twice and therefore, it is certain that the filaments are within the flame's combustion reaction zone. The other level farthest from the burner has an  $HAB=17.7$  mm and only one continuous red pixel area, suggesting that the

filament is at the boundary of the combustion reaction zone or just outside of it; any measurement from this filament will not be representative of the flame's temperature.

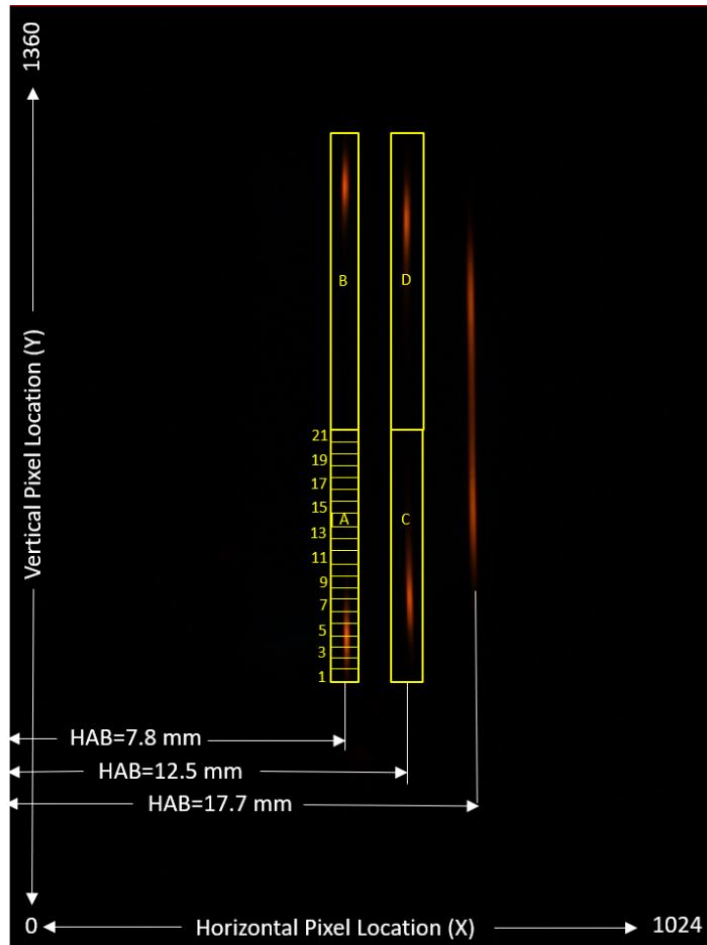


Figure 9: Pixel intensity mapping of a TIFF image

For filament level HAB=7.8 mm, the two separate red pixel areas are labelled as “A” and “B”. For area “A”, there are rows of pixels labelled “1” to “21” (this is for illustration only; in actuality, approximately 400 rows of pixels exist in an area). For each row, the red pixel values are averaged, and out of these averages the peak or maximum is selected and divided by the FF and TF. This value is the local peak pixel that corresponds to the peak temperature

in area “A”. The same procedure is done for area “B” and the average of the two local peak pixels is essentially the I that is used for the computation of  $T_{fil}$  using Eq. 3. The same procedure is used for area “C” and “D” to determine the pixel intensity for level HAB=12.5 mm. The HAB=17.7 mm is disregarded because it is non-representative.

### 2.1.5. Temperature Correction

The computed filament temperature is expectedly lower than the actual gas temperature ( $T_{gas}$ ) because of losses to surroundings. To account for these losses, a steady-state heat balance for a gas and cylindrical filament is assumed, as summarized in Eq. 4 below (Maun, Sunderland and Urban, 2007).

$$h(T_{gas} - T_{fil}) = \sigma \epsilon_{fil} (T_{fil}^4 - T_{amb}^4) - \left( \frac{k_{fil} d_{fil}}{4} \right) \frac{d^2 T_{fil}}{dx^2} \quad (4)$$

The term at the left side of the equation is convective heat transfer. At the right side, the first term is radiative heat transfer, and the second term is conductive. However, because the filament has small diameter ( $d_{fil}$ ) and thermal conductivity ( $k_{fil}$ ), the conductive term can be neglected. Additionally, the convective heat transfer coefficient ( $h$ ) in W/m<sup>2</sup>-K is calculated from the Nusselt number (Nu), the ratio of convective and conductive heat transfer across a fluid boundary, using  $h = \frac{k_{gas}}{d_{fil}} Nu$ . Then, an empirical correlation of Nu is determined to arrive at the expression of  $h = \frac{k_{gas}}{d_{fil}} \left[ 0.8237 - 0.5 \ln \left( \frac{u_{gas} d_{fil}}{\alpha_{gas}} \right) \right]^{-1}$ . After

inputting this expression to Eq. 4 and transposing, the final equation to compute for  $T_{\text{gas}}$  is shown below.

$$T_{\text{gas}} = T_{\text{fil}} + \frac{\sigma \epsilon_{\text{fil}} d_{\text{fil}} (T_{\text{fil}}^4 - T_{\text{amb}}^4) \left[ 0.8237 - 0.5 \ln \left( \frac{u_{\text{gas}} d_{\text{fil}}}{\alpha_{\text{gas}}} \right) \right]}{k_{\text{gas}}} \quad (5)$$

The  $\sigma$  is the Stefan-Boltzmann constant ( $5.67 \times 10^{-8} \text{ W/m}^2\text{-K}$ ). For the filament's properties,  $T_{\text{fil}}$  is the previously calculated filament temperature in K,  $\epsilon_{\text{fil}}$  is 0.88 and  $d_{\text{fil}}$  is  $1.4 \times 10^{-5} \text{ m}$ . For the gas properties, the  $u_{\text{gas}}$  is velocity (0.01 m/s), while the  $\alpha_{\text{gas}}$  ( $\text{m}^2/\text{s}$ ) is thermal diffusivity, and  $k_{\text{gas}}$  ( $\text{W/m-K}$ ) is thermal conductivity of Nitrogen (a simplification because the majority of the gas in the system is Nitrogen) computed at the mean of  $T_{\text{gas}}$  and  $T_{\text{fil}}$ , both in K. Lastly the ambient temperature  $T_{\text{amb}}$  is given as 298 K.

The temperature correction, together with intensity conversion in the previous section, was executed using Matlab which can easily differentiate the various color channels, map the pixel locations in each channel, determine pixel intensity in each location, and perform computations with these variables in an efficient, iterative manner. In addition, a graphics generation functionality is available to readily visualize results.



### 2.3. CEA Gas Temperature Determination

Equilibrium temperatures were calculated for the flames using Chemical Equilibrium with Applications (CEA) program, a tool developed by NASA to analyse combustion and rocket systems using equilibrium chemical thermodynamic properties (NASA, 2021). In the program, the overall chemical composition of the reactants is specified; these are at stoichiometric ratio of fuel and oxygen for all BRE flames. In addition, two independent thermodynamic variables are held constant, in this case, the pressure and enthalpy, to solve for the temperature.

The reaction parameters used in calculating the equilibrium temperature are summarized in Table 3. The combustion reaction is represented by this equation:  $C_2H_4 + 3O_2 + n_{N_2}N_2 \rightarrow 2CO_2 + 2H_2O + n_{N_2}N_2$ . The reactions are set at stoichiometric ratio of 1 mole of  $C_2H_4$  for every 3 moles of  $O_2$ , and the  $n_{N_2}$  or moles of  $N_2$  (accounting for the oxygen diluent and the fuel diluent) is varied. In addition, the reaction chamber pressure is also a variable.

In the CEA calculation, a relationship between the equilibrium temperature and radiative loss fraction ( $X_r$ ) was established for all the flames by assuming progressive enthalpy losses from the maximum possible enthalpy of the stoichiometric mixture. This relationship, expressed as a polynomial equation, was then used to compute for the “CEA gas temperatures” to differentiate from the “TFP gas temperatures” calculated from TFP.

To elaborate, the input data for the calculation of the CEA gas temperatures are the  $X_r$  values calculated from BRE radiometer readings over time, so that the CEA gas temperatures over time can be generated. In summary, the equation for calculating  $X_r$  is given as:  $X_r = \frac{\dot{q}_A}{\dot{q}''}$  where  $\dot{q}''$  is

the radiant heat flux detected by the radiometer in kW/m<sup>2</sup>, A is the effective area in m<sup>2</sup>, and  $\dot{q}$  is the theoretical heat release rate of the stoichiometric reaction in kW.

*Table 3: Reaction parameters of self-extinguished (Flame 1 & 2) and fuel-terminated (Flame 3 & 4) flames*

Flame (Test) Identification	Moles N <sub>2</sub>	Reaction chamber pressure, kPa
Flame 1 (21020D1)	9.8	70
Flame 2 (20358G2)	11.1	101
Flame 3 (21020A1)	7.6	57
Flame 4 (20346A5)	5.9	101


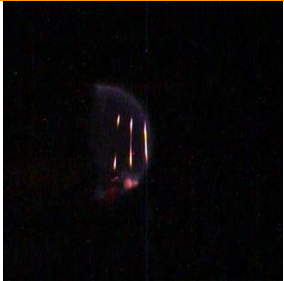



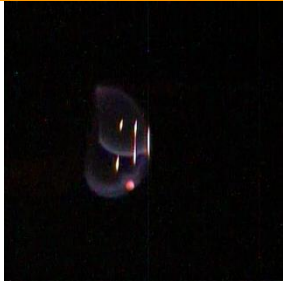

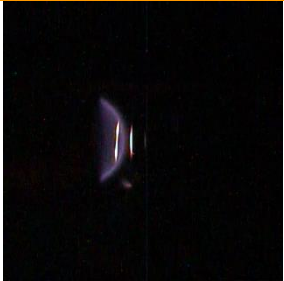


### 3.1. TFP Gas Temperature

Table 4 illustrates the characteristics of the four flames with  $C_2H_4$  fuel and 25 mm burner after the selection process. It shows the screen grab of the videos from the ACME Operations Camera at different time frames and with the burner is positioned sideways at the left. The flame evolution is illustrated right after ignition, after the filaments are inserted and already stationary, and during oscillation.

Of particular interest is the placement of filaments with respect to the flame front; filaments that are located just at the boundary or outside of the flame front are disregarded from the analysis because they are not representative of the combustion zone properties. After observation of the locations, two filaments each for Flame 1 and Flame 2, and only one filament each for Flame 3 and 4 were chosen for TFP.

After flame selection, the raw HOBj images were formatted and subtracted using OMA2, resulting to TIFF images with arrays of pixels that can be processed further. These TIFF images were then inputted in Matlab for the process of intensity conversion to temperature.

Table 4: Evolution of self-extinguished (Flame 1 & 2) and fuel-terminated (Flame 3 & 4) flames

Flame (Test) Identification	Time Frame		
	Right After ignition	After filament insertion	During oscillation
Flame 1 (21020D1)	 $t_{\text{ignition}} + 3.00\text{s}$	 $t_{\text{ignition}} + 17.18\text{ s}$	 $t_{\text{ignition}} + 65.14\text{ s}$
Flame 2 (20358G2)	 $t_{\text{ignition}} + 3.00\text{ s}$	 $t_{\text{ignition}} + 16.89\text{ s}$	 $t_{\text{ignition}} + 31.93\text{ s}$
Flame 3 (21020A1)	 $t_{\text{ignition}} + 3.00\text{ s}$	 $t_{\text{ignition}} + 17.17\text{ s}$	No oscillation
Flame 4 (20346A5)	 $t_{\text{ignition}} + 3.00\text{ s}$	 $t_{\text{ignition}} + 9.93\text{ s}$	No oscillation

Initially, the peak pixel intensities were mapped, screened and quantified. The results of such process are shown in Figure 10 and Figure 11; each of the color represents an image with a unique timestamp. For all the images of a test flame, the peak pixel intensities along the horizontal location were mapped.

Notice that none of the pixels are saturated and the pixels closest to the burner generally have higher values than the other levels. Nevertheless, even if Flame 4 have some pixels that are near-saturation (near the ignition time only), these are further screened out in the subsequent computations when any near-saturation pixels (higher than 95% of the maximum pixel), together with any remnant background noise (less than 8% of the maximum pixel), are disregarded.

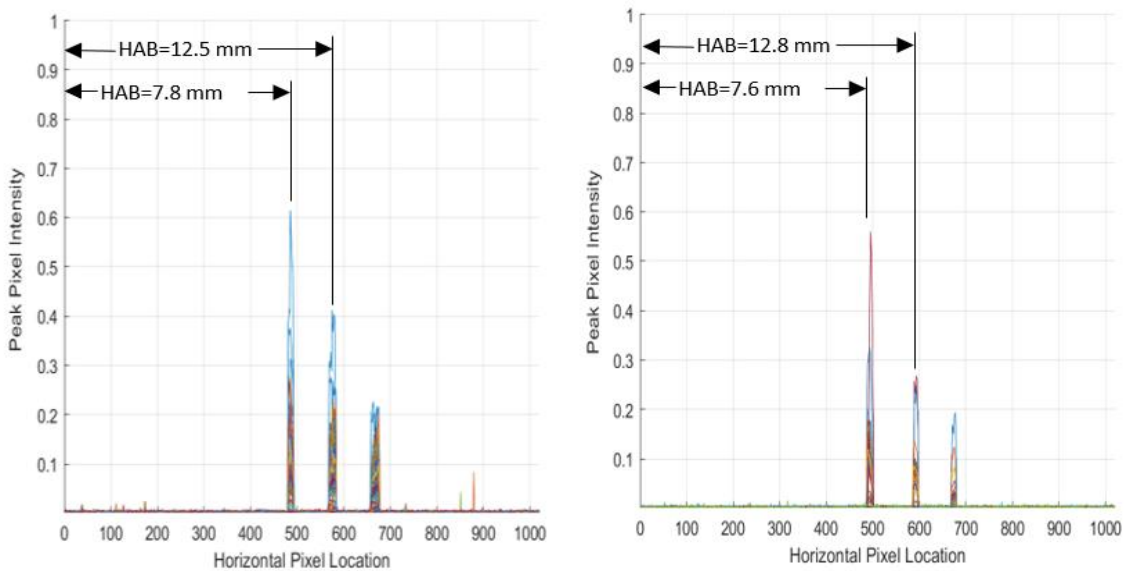
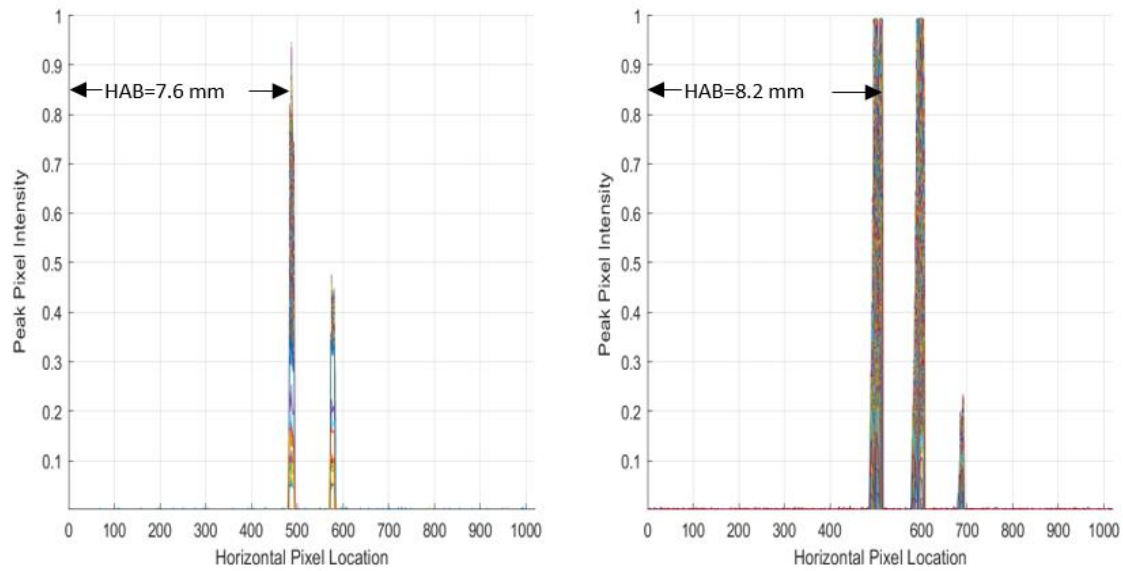


Figure 10: Peak pixel intensity locations for Flame 1 (left) and Flame 2 (right)



*Figure 11: Peak pixel intensity locations for Flame 3 (left) and Flame 4 (right)*

After the peak pixel intensities of the images were quantified, the values were used to compute for the filament temperatures, which were then finally corrected to gas temperatures. Since the images were taken sequentially, the timestamps of these images were used to plot the gas temperatures over time, as shown in the succeeding figures.

For the self-extinguished flames, the gas temperature is highest at the start (near the ignition time) then gradually reduces until the extinction onset when sudden fluctuations in temperature is observed. The temperature reduction is primarily due to gradual increase in radiative losses from the flame to its surroundings as the flame grows over time.

Referring to Figure 12, the highest gas temperatures for Flame 1 are at 1,249 K and 1,241 K for HAB=7.8 mm and HAB=12.5 mm, respectively. For Flame 2 in Figure 13, the highest gas temperatures are 1,217 K (HAB=7.6mm) and 1,194 K (HAB=12.8 mm). For both flames, it can be

observed that the filament closest to the burner (HAB=7.8 mm or HAB=7.6 mm) always have higher gas temperatures than the farther filament.

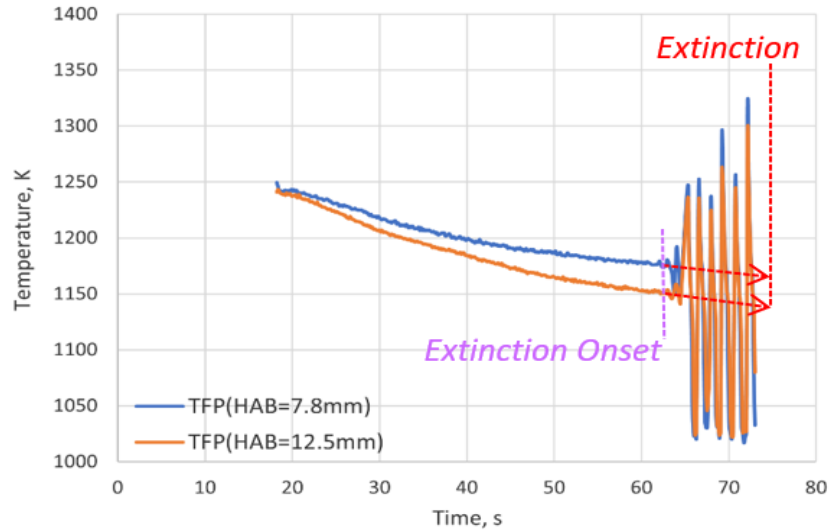


Figure 12: TFP gas temperature over time at different filament levels for Flame 1

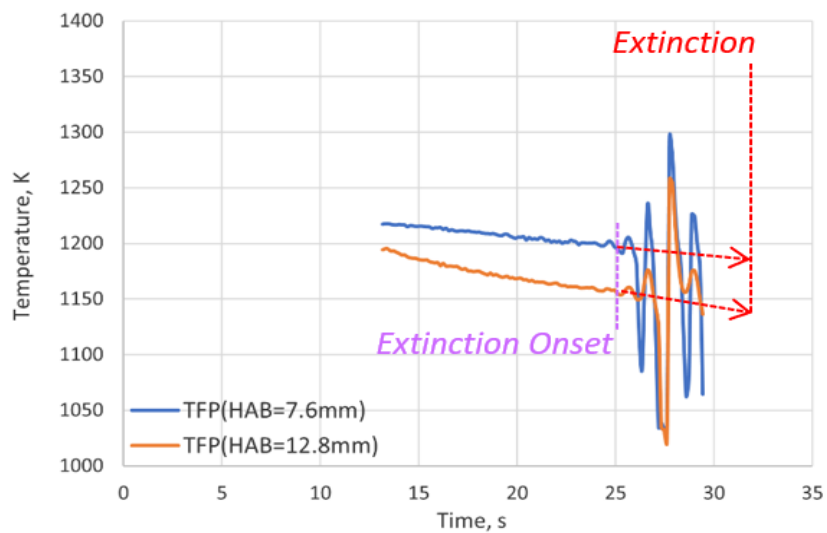


Figure 13: TFP gas temperature over time at different filament levels for Flame 2

At the extinction onset, Flame 1 (Figure 12) has gas temperatures of 1,172 K and 1,149 K for HAB=7.8 mm and HAB=12.5 mm, respectively. On the other hand, Flame 2 (Figure 13) has gas temperatures of 1,197 K (HAB=7.6 mm) and 1,155 K (HAB=12.8 mm). After reaching these temperatures, sudden fluctuations in temperatures continue until the flames extinguish on their own.

Note that after the extinction onset temperature, the instability of the flame causes it to change shape and volume. At some instances, the filaments are not exposed anymore to combustion gases as seen in the drops in temperature. In other instances when the volume recovers, the sudden flashing of gases around the hot filaments are seen as spikes in temperature. This pattern of drops and spikes amplifies progressively until extinction. Furthermore, the intensities near the extinction temperature are too low to be worth quantifying. Consequently, a definite extinction temperature can not be easily identified through TFP.

Nevertheless, linear projection from the point just before oscillation to the extinction time reveals that the projected extinction temperature is 11 K lower than the extinction onset temperature on average. Table 5 summarizes the results of the projections, with  $R^2$  values of 0.7014 and 0.8507 for Flame 1 and Flame 2, respectively. The mean temperatures for both flames are 1,168 K and 1,157 K for the extinction onset temperature and projected extinction, respectively.



*Table 5: Projection of extinction temperature for Flame 1 and Flame 2*

Flame (Test) Identification	HAB, mm	Extinction onset Temperature, K	Projected Extinction Temperature, K	Difference, K
Flame 1 (21020D1)	7.8	1,172	1,166	-6
	12.5	1,149	1,139	-10
Flame 2 (20358G2)	7.6	1,197	1,186	-11
	12.8	1,155	1,140	-15
Average		1,168	1,157	-11

For the fuel-terminated flames, the general trend of peak gas temperature gradually decreasing over time is also observed. However, no fluctuation in temperature is evident. Flame 3 (Figure 14) starts at 1,361 K then progressively reduces to 1,284 K, while it can be observed in Figure 15 that Flame 4 temperature begins to fall steadily from 1,385K until 1,254 K when the fuel is cut-off.

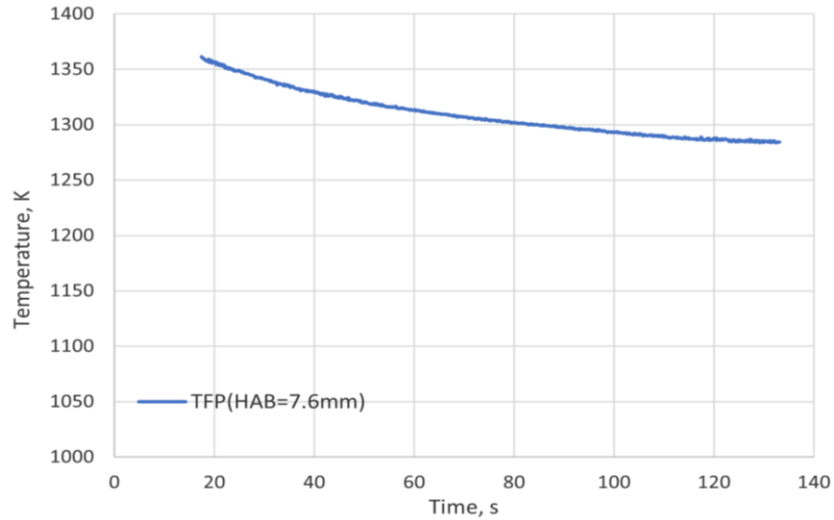


Figure 14: TFP gas temperature over time for Flame 3

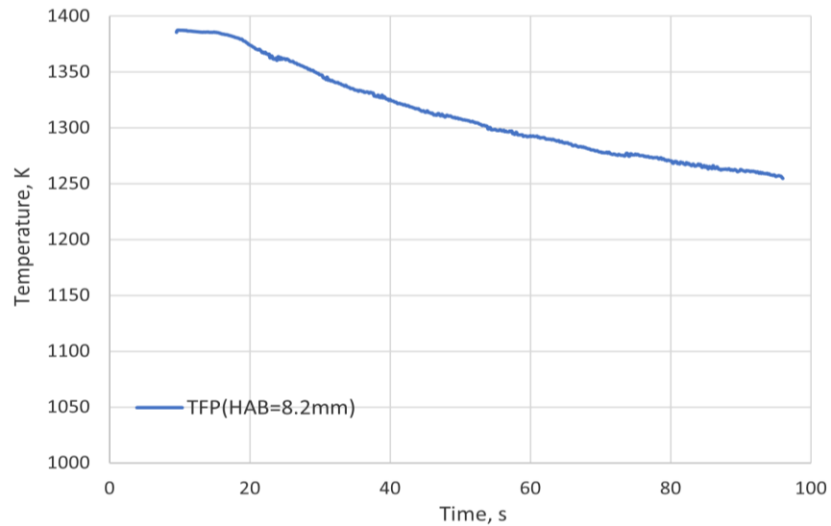


Figure 15: TFP gas temperature over time for Flame 4

### 3.2. CEA Gas Temperature

The equilibrium temperatures as a function of radiative loss fraction ( $X_r$ ) are summarized in Figure 16 and Figure 17. The curve fitting using second order polynomial equation produced acceptable  $R^2$  values of 0.9996-0.9997. Subsequently, these equations, together with the  $X_r$  values computed from radiography readings, were used for plotting CEA gas temperatures over

time. Observe that Flame 4 has the highest equilibrium temperatures over the range of  $X_r$ , chiefly because it has the least moles of  $N_2$  diluent in its combustion reaction, while the effect of pressure is less significant.

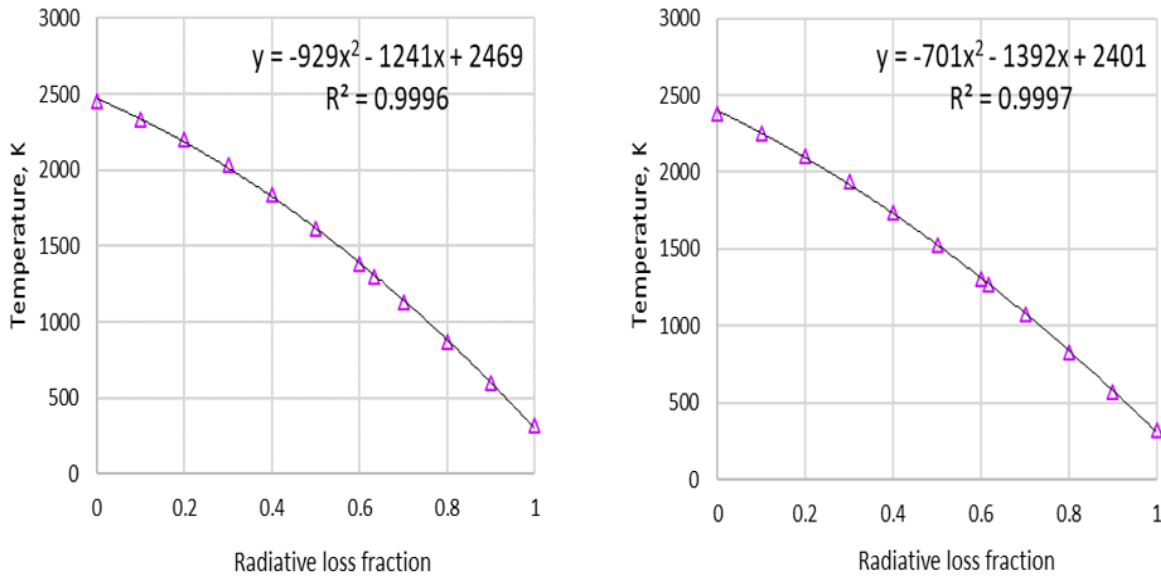


Figure 16: Equilibrium temperature as function of radiative loss fraction for Flame 1 (left) and Flame 2 (right)

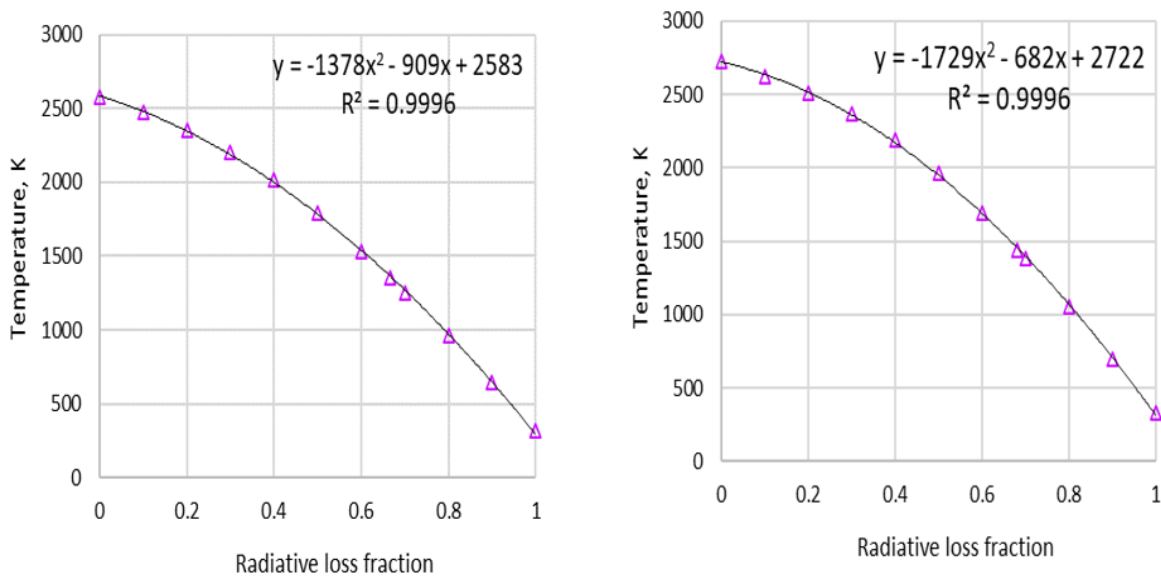


Figure 17: Equilibrium temperature as function of radiative loss fraction for Flame 3 (left) and Flame 4 (right)

The final CEA gas temperatures are plotted over time in Figure 18 to Figure 21. It can be observed that all the flames have CEA gas temperatures that follow the same pattern as the temperatures computed from TFP, although the absolute values are different. The detailed comparison of the CEA gas temperature and TFP gas temperature is discussed in the next chapter.

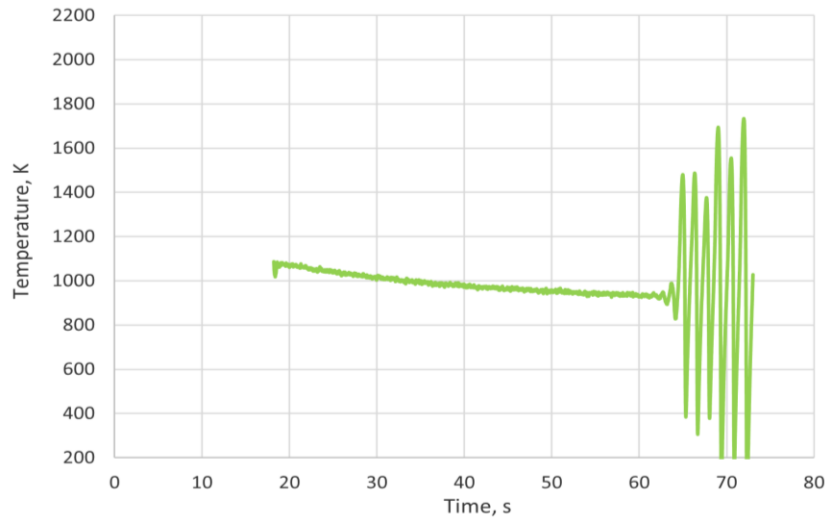


Figure 18: CEA gas temperature over time for Flame 1

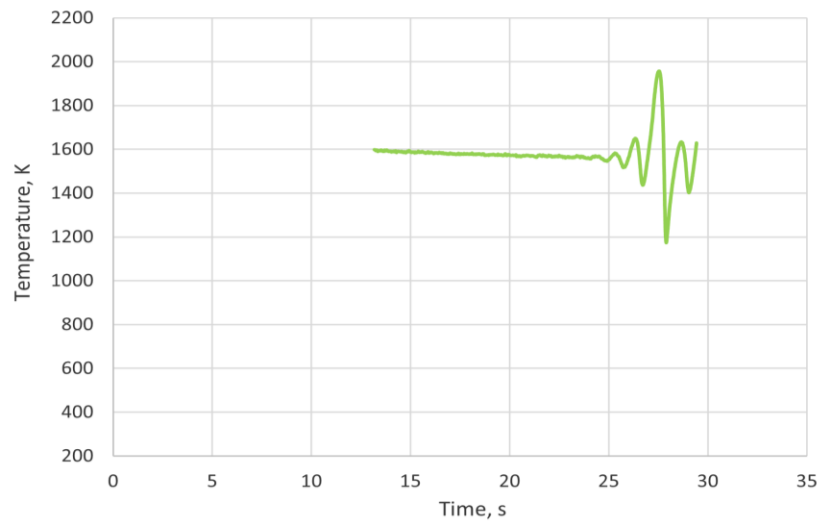
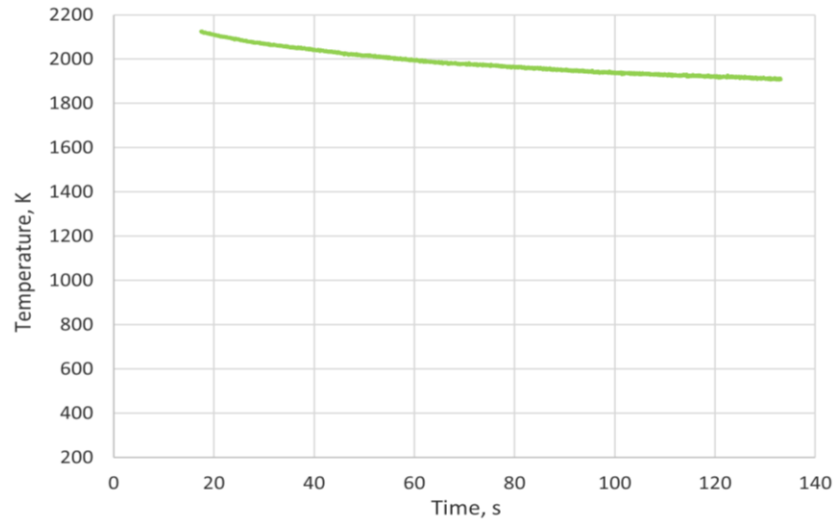
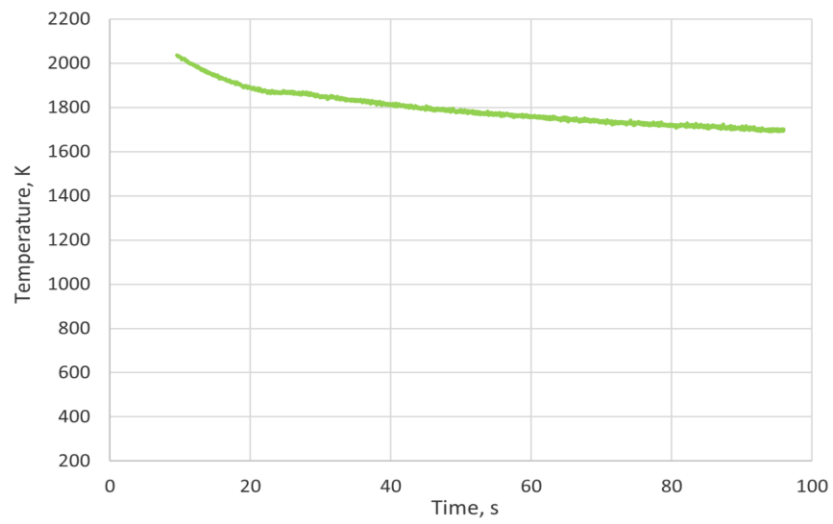


Figure 19: CEA gas temperature over time for Flame 2



*Figure 20: CEA gas temperature over time for Flame 3*



*Figure 21: CEA gas temperature over time for Flame 4*

## Chapter 4 – Discussion

For the self-extinguished flames, the extinction onset temperatures as illustrated previously in Figure 12 and Figure 13 are recapitulated in Table 6 as “Base Case”, with additional “Sensitivity Case” to account for two identified uncertainties in calculation. The first uncertainty is with TF used in the  $T_{fil}$  calculation which is assumed to vary by  $\pm 0.10$  from the numerical best fit value of 0.36. The other uncertainty is from  $u_{gas}$  used in  $T_{gas}$  calculation which may have variation of  $\pm 0.005$  from the simulated value of 0.010 m/s.

*Table 6: Sensitivity analysis of extinction onset temperature for Flame 1 and Flame 2*

Flame (Test) Identification	HAB, mm	Base Case  TF=0.36 $u_{gas}=0.010$ m/s	Sensitivity Case (Difference from Base Case)			
			TF=0.26	TF=0.46	$u_{gas}=0.005$ m/s	$u_{gas}=0.015$ m/s
Flame 1 (21020D1)	7.8	1,172	+21	-15	+5	-3
	12.5	1,149	+21	-14	+5	-2
Flame 2 (20358G2)	7.6	1,197	+22	-16	+5	-3
	12.8	1,155	+21	-15	+5	-2
Average		1,168	+21	-15	+5	-3

The average extinction onset temperature of 1,168 K (base case) has a total uncertainty of -18/+26 K. The uncertainty because of TF is -15/+21 K on average, while  $u_{gas}$  has a lesser contribution of about -3/+5 K.

For all the flames, the comparisons of TFP gas temperature with the CEA gas temperature are illustrated in Figure 22 to Figure 25. Disregarding the oscillation periods, the absolute discrepancies between the two methods are 200 K for Flame 1, 400 K for Flame 2, 700 K for Flame 3, and 500 K for Flame 4. Indeed, the discrepancies are significant and suggest the need to revisit the inputs to the CEA calculations that may have contributed to this.

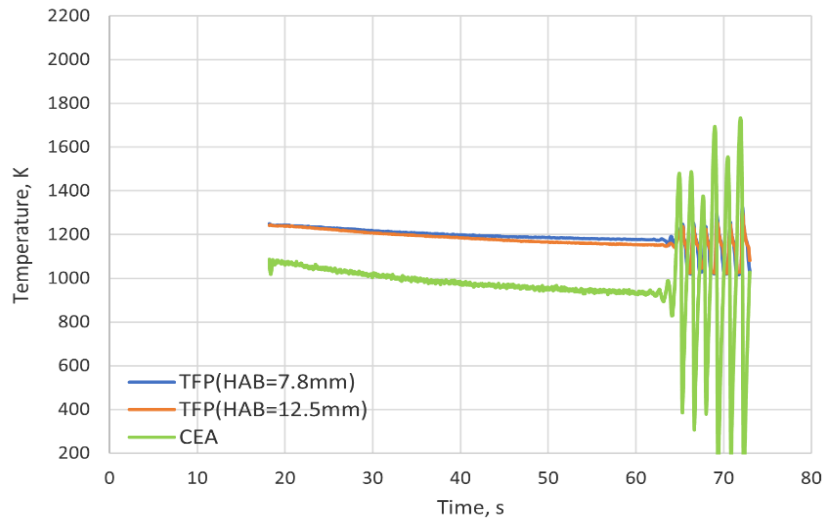


Figure 22: TFP gas temperature comparison with CEA gas temperature for Flame 1

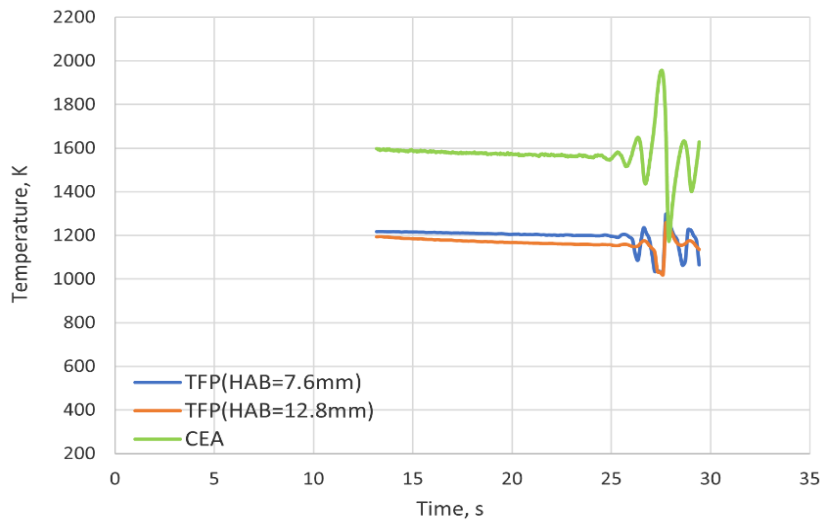


Figure 23: TFP gas temperature comparison with CEA gas temperature for Flame 2

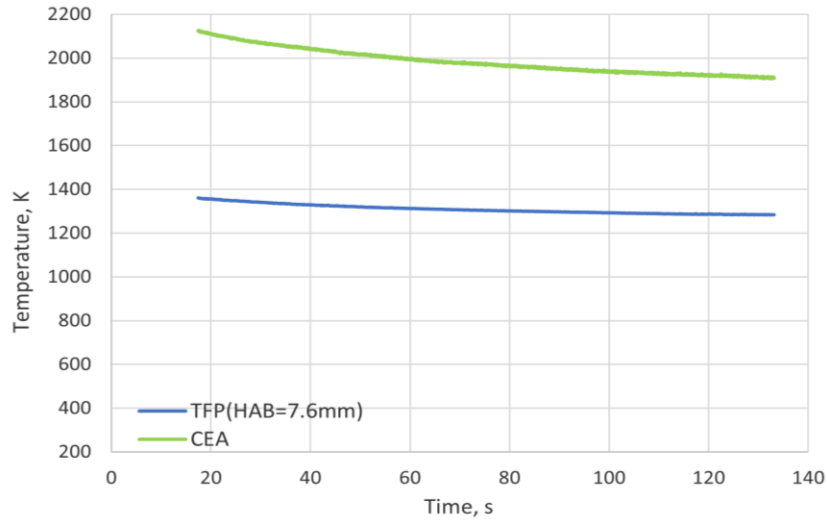


Figure 24: TFP gas temperature comparison with CEA gas temperature for Flame 3

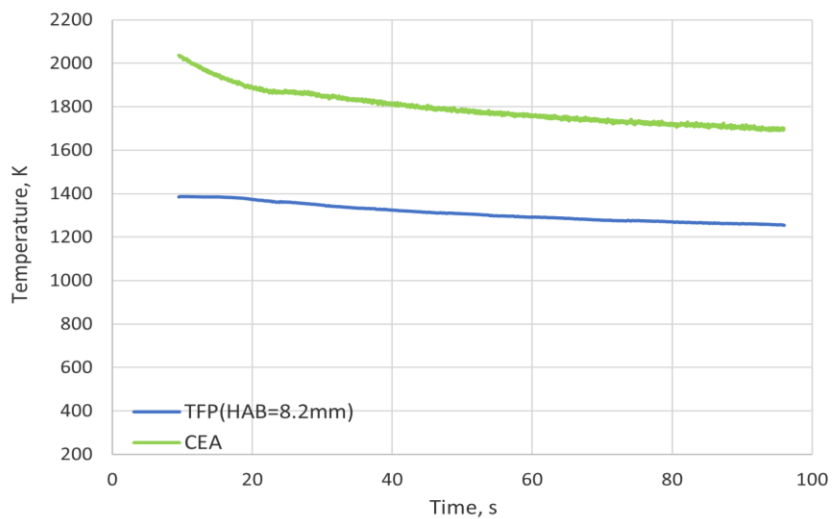
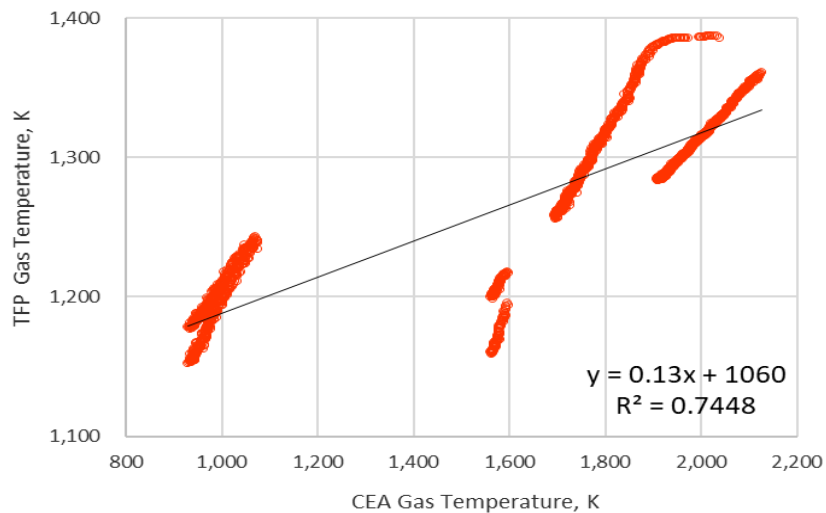


Figure 25: TFP gas temperature comparison with CEA gas temperature for Flame 4

Recall that the CEA temperature was computed from equilibrium temperature equations and  $X_r$  computation. At the outset, the equilibrium temperature equations are based on a well-established heat of combustion value of  $C_2H_4$ , so the equations are straightforward and least likely contributor to the discrepancy. Then, the  $X_r$  calculation consists of three factors:  $\dot{q}''$  and  $A$



from radiometry reading and  $\dot{q}$  from reactants flow readings. These factors must be verified accordingly. For the radiometry, the assumption of burner surface re-radiation and angular orientation from the radiometer to the flame can be revisited. For the flow readings, the possibility of fuel leakage can be explored. However, initial assessment did not identify specific input parameters to the calculation that can be adjusted to minimize the observed discrepancy. Nevertheless, a linear curve fitting of the TFP gas temperature and CEA gas temperature is proposed and shown in Figure 26 . The  $R^2$  value of 0.7448 is still acceptable, so that the “true temperature” can still be approximated just by using the CEA program and  $X_r$  calculations without resorting to the time-consuming and specialized method of TFP.



*Figure 26: TFP gas temperature as a function of CEA gas temperature*

## Chapter 5 - Conclusions

The main objective of this thesis was to answer two fundamental questions about flame in microgravity. The first inquiry on what is the temperature that indicates flame extinction had been answered by values generated from TFP measurement: the extinction onset temperature is 1,168 K with  $-18/+26$  K uncertainty. The TFP measurement is close to the 1,100 K value that was predicted for spherical diffusion flames in a 2.2-s drop tower test, using simulation and TFP (Santa, 2007). Moreover, the TFP measurement agrees with a finding in a previous three-dimensional simulation of BRE flames from round one tests: peak flame temperatures progressively decrease over time to about 1,200 K prior to extinction onset (Snegirev, 2020).

However, the extinction temperature of 1,157 K is merely a projection from the extinction onset temperature because the fluctuating flame characteristic after extinction onset renders the TFP measurement as non-representative of the gas temperature. As such, other measurement techniques to ascertain the extinction temperature must be explored.

The second question on whether the true temperature (or TFP gas temperature) is indicated by radiative loss fraction (used to compute the CEA gas temperature) had been answered with “not exactly”. The gradual reduction of temperature over time, and the timing of extinction onset are comparable. However, there are significant differences of 200-700 K between the TFP-measured temperature and the CEA-calculated temperature that necessitates revisiting inputs to CEA calculation.

With the above findings, a better understanding of fire safety in microgravity is achieved. The finding on the extinction onset temperature can define more precisely and accurately the flammability range of materials used within spacecrafts. Potentially, temperature-activated, flame extinguishing system can be designed to use extinguishing materials more efficiently, especially in resource-limited settings like spacecrafts. On the other hand, the “true temperature” measured from TFP can be used to minimize the uncertainties in other measuring methods. Particularly for radiometry, a curve fitting equation had been proposed to approximate the “true temperature” without employing the more arduous method of TFP.

For future studies related to this thesis, several topics are proposed. Firstly, TFP can be performed on other fuel type ( $\text{CH}_4$ ) and burner type (50-mm diameter) used in the BRE experiment to observe similarities or differences. Less production from  $\text{CH}_4$  of carbon dioxide ( $\text{CO}_2$ ), which has a strong radiation self-absorption tendency, and higher mass flux from 50-mm burner may create flames with different transient temperature behavior and extinction characteristic.

Also, study of flames with periodic oscillation – oscillates repeatedly but do not self-extinguish – can be initiated. The aim is to find out the conditions that sustain such flame characteristic and the mechanism of flame recovery.

Lastly, the TFP method can be fine-tuned using flame simulation that can help validate assumptions and reduce uncertainties. Initially, a simulation has been performed on Flame 1 by Dr. Alexander Snegirev, a BRE research team member from Russia. The simulation result shows some similarities with TFP results, but these are preliminary and warrant further investigation in consideration of the other flame tests as well.

## References

- Çengel, Yunus A. (2007) *Heat And Mass Transfer: a Practical Approach*. 3rd edn. Boston: McGraw-Hill.
- Chao, D. F. , Green, R. D., McQuillen, J. B., Meyer, W. V. and Motil, B. J. (2015) *A Researcher's Guide to: International Space Station Fluid Physics*.
- Chhabra, Raj and Shankar, V. (eds) (2018) 'Heat Transfer', in *Coulson and Richardson's Chemical Engineering*. 7th edn. Elsevier, pp. 3–264. doi: 10.1016/B978-0-08-102550-5.00001-8.
- Dehghani, Parham, Sunderland, Peter B., Quintiere, James G. and DeRis, John L. (2021) 'Burning in microgravity: Experimental results and analysis', *Combustion and Flame*, 228, pp. 315–330. doi: 10.1016/j.combustflame.2021.01.035.
- Franceschetti, Donald R. (ed.) (2012) 'Photography', in *Applied Science*. Massachusetts, New Jersey: Salem Press, pp. 1462–1463.
- Glückert, Udo L. (1994) 'Pyrometry and Thermography', in Mayinger, Franz (ed.) *Optical measurements: techniques and applications*. Berlin: Springer-Verlag.
- Juanós, Albert Jordà and Sirignano, William A. (2014) 'Triple flame: Inherent asymmetries and pentasectional character', *Combustion Theory and Modelling*, 18(3), pp. 454–473. doi: 10.1080/13647830.2014.923116.
- Kalt P.A.M., Long M. B. (2019) *OMA – Image processing for Mac OS X*. Available at: <http://oma-x.org/oma2WebPage/index.html>.
- Kuhn, Peter B., Ma, Bin, Connelly, Blair C., Smooke, Mitchell D. and Long, Marshall B. (2011) 'Soot and thin-filament pyrometry using a color digital camera', *Proceedings of the Combustion Institute*, 33(1), pp. 743–750. doi: 10.1016/j.proci.2010.05.006.
- Lecoustre, Vivien R., Narayanan, Praveen, Baum, Howard R. and Trouvé, Arnaud (2011) 'Local extinction of diffusion flames in fires', *Fire Safety Science*, pp. 583–595. doi: 10.3801/IAFFS.FSS.10-583.
- Ma, Bin, Wang, Guanghua, Magnotti, Gaetano, Barlow, Robert S. and Long, Marshall B. (2014) 'Intensity-ratio and color-ratio thin-filament pyrometry: Uncertainties and accuracy', *Combustion and Flame*, 161(4), pp. 908–916. doi: 10.1016/j.combustflame.2013.10.014.
- Markan, Akshit, Sunderland, Peter B., Quintiere, James G., de Ris, John L., Stocker, Dennis P., Baum, Howard R. (2018) 'A Burning Rate Emulator (BRE) for study of condensed fuel burning in microgravity', *Combustion and Flame*, 192, pp. 272–282. doi: 10.1016/j.combustflame.2018.01.044.

Markan, Akshit, Baum, Howard R., Sunderland, Peter B., Quintiere, James G. and de Ris, John L. (2020) 'Transient ellipsoidal combustion model for a porous burner in microgravity', *Combustion and Flame*, 212, pp. 93–106. doi: 10.1016/j.combustflame.2019.09.030.

MathWorks (2021) *Matlab*. Available at: <https://mathworks.com/products/matlab.html>.

Maun, Jignesh D., Sunderland, Peter B. and Urban, David L. (2007) 'Thin-filament pyrometry with a digital still camera', *Applied Optics*, 46(4), pp. 483–488. doi: 10.1364/AO.46.000483.

NASA (2013) 'ACME-SRD-001.B Integrated Science Requirements Document (ISRDR)', *Advanced combustion via microgravity experiments*.

NASA (2016) *ACME-RPT-010 A, Data Camera Characterization Report*.

NASA (2020) *Mars 2020 Mission Overview*. Available at: <https://mars.nasa.gov/mars2020/mission/overview/>.

NASA (2021) *Chemical Equilibrium with Applications (CEA)*. Available at: <https://cearun.grc.nasa.gov/>.

Santa, K. J., Chao, B. H., Sunderland, P. B., Urban, D. L., Stocker and D. P., Axelbaum, R. L. (2007) 'Radiative extinction of gaseous spherical diffusion flames in microgravity', *Combustion and Flame*, 151(4), pp. 665–675. doi: 10.1016/j.combustflame.2007.08.009.

Snegirev, Alexander, Kuznetsov, Egor, Markus, Ekaterina, Dehghani, Parham and Sunderland, Peter (2020) 'Transient dynamics of radiative extinction in low-momentum microgravity diffusion flames', *Proceedings of the Combustion Institute*, 38(3), pp. 4815–4823. doi: 10.1016/j.proci.2020.06.110.

Stocker, Dennis P., Takahashi, Fumiaki, Hickman, J Mark and Suttles, Andrew C. (2014) 'Gaseous Non-Premixed Flame Research Planned for the International Space Station', pp. 1–13.

Vilimpoc, V. and Goss, L. P. (1988) 'SiC-Based Thin-Filament Pyrometry: Theory and Thermal Properties', in *Twenty-Second Symposium (International) on Combustion / The Combustion Institute*, pp. 1907–1914.

Zhang, Yi, Kim, Matt, Guo, Haiqing, Sunderland, Peter B., Quintiere, James G., DeRis, John and Stocker, Dennis P. (2015) 'Emulation of condensed fuel flames with gases in microgravity', *Combustion and Flame*, 162(10), pp. 3449–3455. doi: 10.1016/j.combustflame.2015.05.005.